

Studying beam position measurements for the luminosity calibration at CMS

Maarten De Coen

Academic year 2021–2022



**GHENT
UNIVERSITY**

Department of Physics and Astronomy
Experimental Particle Physics

**Studying beam position measurements for the
luminosity calibration at CMS**

Maarten De Coen

Promotor **Prof. Dr. Didar Dobur**
Department of Physics and Astronomy
Ghent University

Supervisor **Dr. Joscha Knolle**
Department of Physics and Astronomy
Ghent University

Master's thesis submitted in partial fulfilment of the requirements for obtaining the
academic degree of Master of Physics and Astronomy

Academic year 2021–2022

Maarten De Coen

Studying beam position measurements for the luminosity calibration at CMS

Academic year 2021–2022

Promotor: Prof. Dr. Didar Dobur

Supervisor: Dr. Joscha Knolle

Ghent University

Experimental Particle Physics

Department of Physics and Astronomy

Sint-Pietersnieuwstraat 25

9000 Ghent

Abstract

Modern particle physics relies heavily on colliders to push the limits of our understanding ever further. The largest and most powerful one among them is the LHC, run by CERN in Geneva (Switzerland). One crucial parameter expresses the power of these colliders: luminosity. It tells us how many collisions we can generate and is essential to determine cross-sections. Measuring luminosity is, however, complicated in hadron colliders. The method of choice at LHC is the Van Der Meer method, which has allowed for an unprecedented accuracy at the per cent level. The characteristic of this method is that the colliding particle beams move away from a head-on collision course. However, our imperfect knowledge of the beam positions is also one of the main limitations on the accuracy today. In this thesis, I address this issue by studying beam position measurements with an at CERN unprecedented level of detail. I have modelled known phenomena affecting the beam positions and looked for new ones in the data. Finally, I quantified the effects of these phenomena on the luminosity measurement and the uncertainty they introduce.

Samenvatting

Moderne deeltjesfysica is sterk afhankelijk van colliders om de grenzen van onze kennis steeds verder te verleggen. Op dit moment is de grootste en krachtigste onder hen de LHC, gerund door CERN in Genève (Zwitserland). Eén cruciale parameter drukt de kracht uit van deze versnellers: luminositeit. Ze vertelt ons hoeveel botsingen we kunnen opwekken, en is essentieel om werkzame doorsnedes te bepalen. Een luminositeitsmeting is echter een ingewikkeld probleem in hadronversnellers. De geprefereerde methode voor LHC is de Van Der Meer methode. Die heeft het mogelijk gemaakt een onovertroffen nauwkeurigheid te bereiken op het percent niveau. Typisch voor deze methode is dat de botsende deeltjesbundels weg bewegen van de frontale botsingskoers. Echter, onze kennis van de bundelposities is niet perfect, wat vandaag de dag een van de voornaamste beperkingen is op de precisie. In dit proefstuk pak ik dit probleem aan door de positiemetingen van de bundel te bestuderen met een tot nog toe in CERN ongeziene nauwkeurigheid. Ik heb de gekende fenomenen gemodelleerd die de bundelposities beïnvloeden en gezocht naar nieuwe in de data. Ten slotte heb ik de effectgrootte van die fenomenen becijferd samen met de onzekerheid die ze introduceren in de luminositeitsmeting.

Acknowledgement

This document represents a lot of work and effort over the last year. If I had been alone on this journey, it would have been most likely in vain. I want, therefore, to thank all the people who helped me successfully arrive at this point.

First of all, many thanks to Didar for providing me with this opportunity in the first place. Last year, when I was in much doubt about which way to go, she was the one to convince me in this direction. She always encouraged and believed in me, which I am eternally grateful for, especially given my own regular lack of self-confidence.

I am no less thankful to Joscha, who really dragged me through this with unbelievable energy and unrelenting support. He provided me with wonderful opportunities in the CMS collaboration, which I could not have imagined upfront. On top of that, he has been great company in between work. I could not have wished myself a better supervisor.

Furthermore, I want to thank all the members of the particle physics group in Ghent for having me, a mere master's student, in their company, even all the way up to Switzerland. They are fantastic and welcoming people whom I would warmly recommend to anyone.

Many thanks to all my friends for providing a way out of my university work and keeping me sane. I am especially indebted to all who were willing to listen to what this whole thesis is actually all about. I would specifically want to acknowledge Alina. She not only had the patience to hear me explaining my work in some language that hopefully somewhat resembled Russian. She also read and commented on this entire thesis for me.

Finally, special thanks to Andreas for allowing me to attend the weekly BRIL/Lumi meetings and be a part of the general luminosity activities at DESY. Thanks to Christoph for answering my questions about the LHC instrumentation and magnets. Thanks also to prof. Van Steelandt for his great course on linear regression and his help on that topic for my master thesis.

Contents

Introduction	1
1 Particle Physics	5
1.1 A particle zoo	5
1.2 The physics of particles	7
1.2.1 Special relativity	7
1.2.2 Quantum mechanics	8
1.2.3 The standard model of particle physics	8
1.3 Accelerators	10
1.3.1 The target	10
1.3.2 The shape	11
1.3.3 The particles	11
1.4 CERN and the Large Hadron Collider	12
2 Large Hadron Collider	15
2.1 Overall structure	15
2.2 Proton bunches	16
2.3 Beam currents	17
2.4 Beam positions	18
2.5 Beam optics	19
3 Luminosity	23
3.1 What is luminosity	23
3.2 Why luminosity matters	24
3.3 Theory of luminosity	25
3.4 Measurement	28
3.4.1 From machine parameters	28
3.4.2 From a known cross-section	29
3.4.3 The Van Der Meer Method	29
4 The Van Der Meer Method	31
4.1 Luminometers	31

4.2	The VdM integral	32
4.3	Displacing the beams	33
4.3.1	Length scale and misalignment	34
4.3.2	Coherent beam-beam effects	34
4.3.3	Unexplained deviations	36
4.4	The VdM fill	37
4.4.1	Emittance scans	38
4.4.2	Van Der Meer scans	38
4.4.3	Off-set scan	38
4.4.4	Beam Imaging scan	39
4.4.5	Length scale scans	39
4.5	The CMS luminosity measurement from 2015-2016	40
5	Beam Position Monitor Studies	43
5.1	The data	43
5.2	Effects	44
5.3	Orbit drift	46
5.4	Length scale	47
5.5	Misalignment	51
5.6	Beam-beam deflection	51
5.7	Residuals	54
6	A rudimentary Van Der Meer analysis	57
6.1	Vertex counts	57
6.2	Without corrections	58
6.3	Linear orbit drift	60
6.4	Beam-beam deflection	60
6.5	Residuals	60
6.6	Fill 6868	63
	Conclusion and outlook	65
	Bibliography	69
A	Beam position monitors data	83
A.1	Beam positions during fill 6016	83
A.2	Beam positions during fill 6868	84
	Declaration	89

Introduction

“ *It was the best of times, it was the worst of times, it was the age of wisdom, it was the age of foolishness, it was the epoch of belief, it was the epoch of incredulity, it was the season of light, it was the season of darkness, it was the spring of hope, it was the winter of despair.*

— **Charles Dickens**
English writer

Once upon a time, the study of the universe belonged to the realm of philosophy and theology. From the sun shining in the sky and the violence of a stormy sea to the beating of a human heart: humanity watched, pondered, and theorised, resulting in a complicated web of ideas with often little bearing on actual reality. Until around the seventeenth century, a different approach was born. This approach did not aim for a theory that only describes what one passively observes. Instead, it sought a theory predicting everything that should be observable. That imposed a new task on the scientist: the experiment.

Together with the experiment came the science of physics. First, this meant studying falling objects, flowing fluids and stretched strings. This oldest form of physics was later complemented by other fields, like electromagnetism and thermodynamics. As time progressed, knowledge grew, and technology improved, the experiments became more and more involved, measuring Nature’s properties at ever smaller or bigger scales and with higher accuracy. Eventually, they uncovered phenomena unexplainable by the classical theories, which led to a complete overhaul of physics early in the twentieth century. It was during this exciting time the field of particle physics was born.

As the name suggests, particle physics concerns the study of “particles”: point-like objects that make up the world around us. The idea of a particle universe is quite old. In ancient Greek, there was an entire philosophical school championing this idea, called “atomism” from the Greek word *ἄτομος* meaning “indivisible” [1]. According to its members, the universe is a consequence of how these particles or atoms

interact. They rejected all divine or teleological principles upheld by other schools. In this respect, their reasoning was surprisingly similar to the modern scientific point of view.

However, the atom turned out less indivisible than the name suggests. The famous experiments by Ernest Rutherford showed that the atom is a tiny positively charged nucleus orbited by a much larger cloud of negatively charged particles called electrons [2]. That same Rutherford later showed that the nucleus itself was not a point but contained positive particles, which he first interpreted as positively charged hydrogen atoms but later came to be known as protons [3]. In the same period, scientists discovered other particles in cosmic radiation: showers of particles that arise when highly energetic particles coming out of space hit the Earth's atmosphere. Those particles include the positron [4], muon [5], and plenty of other particles.

The study of these particles constitutes the essence of particle physics. This scientific discipline asks what kind of particles are out there, what properties they have, and how they interact with each other. Ultimately, from the atomist point of view, this amounts to questioning the very essence of Nature and pursuing the most fundamental form of scientific knowledge. But studying particles has become increasingly difficult over time. In the early days of particle physics, one could attribute discoveries to just a handful of scientists. Moreover, one could use relatively small-scale analogue detectors, such as cloud chambers and photographic plates.

Starting from the fifties, it became necessary to adopt digital methods due to an increasing need for higher amounts of data. This decade also saw the introduction of the first large-scale accelerators like the cosmotron in Brookhaven (USA). Those devices could accelerate particles to energies that are only naturally seen in cosmic rays, but unlike those natural sources, they could provide a much larger and controllable production rate. The growth in size and technological complexity of experiments forced physicists to work together in ever greater numbers. As a result, the study of the smallest entities in Nature has led to the most large-scale experiments in size, technology, and human resources.

This marriage between the big and the small is nowadays best embodied by the CERN institute in Switzerland. The name, an acronym for *Conseil Européene pour la Recherche Nucleaire*, refers to its original goal when it was conceived in 1952: a centre for the study of the atomic nucleus. But since then, its focus has shifted to the study of fundamental particles. It operates the largest and most powerful human-made particle accelerator to date, the Large Hadron Collider (LHC), which speeds up protons up to an energy of 7 TeV or only 1×10^{-6} % less than the speed of light [6, 7]. These protons typically move in bunches of about 1×10^{11} particles,

which corresponds to the mass of a small bacterium. The energy of such a bunch will be about 100 kJ which is comparable to a car driving on a highway. To achieve that it needs a 27 km long ring inside a 6.5 T strong magnetic field (a thousand times stronger than a typical fridge magnet).

At several points along the LHC's ring, protons circulating in opposite directions meet each other, resulting in a destructive collision. The debris flying outwards is recorded in specialised detectors that are themselves of mind-boggling size. The data analysis then tries to answer two central questions: what type of collisions are there, and how often do they occur? Theoretical models can make predictions for these questions by postulating the existence of certain particles and assuming interactions between them of a certain form and strength. The experiment can then test these theoretical predictions, showing us which theories work and which do not.

There is, however, one decisive factor in answering the second “how often” question that does not depend on fundamental physics. If we halve the number of protons per bunch, the collision number will lower by about the same factor. If we squeeze the protons in a bunch closer together, then collisions will happen more frequently. In other words, the experimentalist has control over the collision rate through the design of the accelerator, which means the absolute number of a given collision is by itself not that meaningful. One would want to compare this to the number of collisions that, hypothetically, would be maximally achievable. This hypothetical number, called *luminosity*, is the central topic in this thesis. Luminosity tells us in a way how intense the proton beams collision-wise are.

Measuring luminosity is thus of paramount importance to the success of any accelerator experiment. Doing this is non-trivial as it requires knowing where the protons are moving inside the accelerator. It is especially difficult to make a precise measurement. At CERN, luminosity is determined through a specialised procedure named after its inventor Simon Van Der Meer [8, 9]. In the past, this method has already enabled luminosity measurements with unprecedented precision compared to other LHC-like colliders [10–18]. However, the remaining uncertainty is still too large and limits the measuring precision for some important physics-related phenomena [19–21]. For this reason, CERN invests a lot of effort in improving the Van Der Meer method.

One key feature of the Van Der Meer method is that the proton beams are moved away from their head-on collision course. That makes the collision rate go down, and how this happens tells us what the luminosity is. However, such manoeuvres introduce uncertainty in the actual position of the beams. Several effects make our

knowledge of the position imprecise if one does not account for them. However, direct position measurements indicate there might be more happening than of which we are aware. That makes the position uncertainty one of the dominant ones.

In this thesis, I present the results of a study of the beam positions. I have analysed the data of direct position measurements based on the effects we know and searched for a sign of yet unknown phenomena affecting the beam positions. All of this I describe in chapter 5. In chapter 6, I use that knowledge to perform a VdM scan analysis and apply concrete corrections to the beam positions. The preceding chapters provide some background information concerning my analysis. Chapter 1 will sketch the broader scientific context of this thesis. It gives an overview of the current status of the field of experimental particle physics and how CERN contributes to it. In chapter 2, I discuss some details about the workings of LHC required to understand the luminosity measurement. Chapter 3 provides a conceptual discussion of luminosity itself and discusses methods to determine it experimentally. The method used at LHC is explained in depth in chapter 4, which also discusses what limits its precision.

Particle Physics

1

” *The world of the quark has everything to do with a jaguar circling in the night.*

— **Arthur Sze**
American poet

1.1 A particle zoo

To the human eye, almost all materials appear to be continuous. In reality, the world is more like a lego structure in which the lego are tiny particles called atoms. Sometimes those atoms are just by themselves, but usually, they are bound to other atoms. Atoms can bind in small groups to form a so-called molecule or gather in astronomical amounts in crystalline structures.

Atoms can bind this way because of their substructure. They are composite objects containing a heavy nucleus orbited by a cloud of electrons. The force keeping the electrons near the nucleus is electromagnetic: the nucleus is positively charged and attracts the negatively charged electrons. When multiple atoms come together, they can start sharing electrons, which results in an electromagnetic bond.

For electrons, there is still no indication that they are composite [22]. Most atomic nuclei, on the contrary, consist of two smaller particles of almost equal mass but with a different charge: the proton (positive) and the neutron (neutral). Like atoms make molecules, neutrons and protons make nuclei. But the force holding them together cannot be electromagnetic as neutrons have no charge. This new kind of force is called the strong nuclear force.

One atom has a single proton for a nucleus: the hydrogen atom. Single neutrons can occur too but will transform into a proton after about fifteen minutes. During this transformation, called negative beta-decay, the neutron ejects an electron together with another neutral particle with a nearly negligible mass: a neutrino. Beta-decay arises because of a third force, different from the electrical and the strong. Since it is much weaker than the other two forces, it goes by the name of the weak force.

In some cases, protons bound in nuclei can also transform into neutrons. This transformation is then positive beta-decay because it results in a neutrino and a positron, a particle identical to the electron but for its positive charge. The existence of the positron is the result of a more general principle in Nature: for any particle, there exists a so-called anti-particle. A particle and its anti-particle are identical in almost all aspects. Only their charges have opposite signs.

The particles introduced above fall into two classes: hadrons and leptons. Hadronic particles like the proton and neutron are subject to the strong force, while leptonic ones like the electron and neutrino are not. Their names come from the Greek $\acute{\alpha}\delta\epsilon\rho\omicron\varsigma$ (thick) and $\lambda\epsilon\pi\tau\acute{\omicron}\varsigma$ (thin), which refers to the observation that hadrons are generally much heavier than leptons.

There are only twelve leptons: the electron, the muon and the tau lepton, three associated neutrinos, and their anti-particles. On the other hand, the hadrons contain a rich spectrum of different particles, such as pions, sigma baryons, omega baryons etc. The enormous variety of hadrons was difficult to digest for physicists of the 20th century. Most physicists intuitively believe that Nature at its smallest, most fundamental level should be elegant and simple. Such a “particle zoo”, as the theoretical physicist Oppenheimer called it somewhat condescendingly, did not fit that intuition [23].

And indeed, all hadrons are made of a handful of smaller particles called quarks. Excluding the anti-particles, there are only six, but the two lightest ones, the up and down quarks, dominate the matter around us. For instance, two up quarks and one down quark make up a proton, while one up quark and two down quarks create a neutron.

As far as we know today, quarks and leptons, or fermions collectively, are fundamental particles. I.e. no experiment shows any indication that they would have any substructure [22, 24]. Together, the fermions make up all the matter around us by interacting through the four basic forces or interactions: the electromagnetic, the weak, the strong, and the gravitational interactions. These interactions work by exchanging yet another type of particle called a boson. In some sense, these bosons work as “messenger” particles mediating the “talking” between interacting particles. Each interaction has its own set of bosons: the photon for the electromagnetic interaction, the Z and W bosons for the weak interaction, and the gluon for the strong interaction. We don’t yet know whether such a boson exists for the gravitational interaction.

1.2 The physics of particles

The previous section has presented particles in an intuitive way, but their description requires mathematical techniques that are difficult to understand based on day to day experience. At these small scales and high energy, intuitive concepts like time and place or the idea of a particle lose their usual meaning. To some physicists, particles are purely mathematical, abstract notions, and only their influence on our observations is what counts. Such physicists would colourfully express this idea with the mantra “shut up and calculate!”. This “calculate” entails two central notions: special relativity and quantum mechanics.

1.2.1 Special relativity

Essentially, special relativity is the mathematical theory of high speed. When objects accelerate to speeds far beyond what humans are used to, they start defying common human understanding. For instance, such an object will look contracted, and its time will appear to run slower to someone at rest. These bizarre phenomena are consequences of another unintuitive principle: light always moves at the same speed c . I.e. a ray of light moving passed you will move at that same speed c , no matter how fast you move.

Albert Einstein was the first who came up with the revolutionary theory from above [25, 26]. The importance of his work is reflected in the fame his name has acquired. And although outside of the physics community, only a few know the exact content of special relativity, almost everyone knows the famous formula $E = mc^2$. This formula establishes the equivalence of mass m and energy E : mass can transform into energy and vice versa according to $E = mc^2$. That is, for instance, why we can generate energy through nuclear fission: when some heavy nuclei split into smaller ones, some mass will convert into energy.

The opposite conversion, energy to mass, is essential to understanding modern particle physics experiments. For instance, if two light particles of mass m hit each other at high speed, they can merge and form a new particle of mass M larger than $2m$. The excess mass comes from the kinetic energy of the original particles. The newly formed particle might be unknown, or we may not yet understand its properties. For this reason, particle physicists take great interest in these types of collision processes.

1.2.2 Quantum mechanics

The second ingredient needed to describe particles is quantum mechanics: the theory of Nature at small scales. As humans, we are used to the deterministic behaviour of simple objects. If you throw a ball, it will take a perfectly predictable orbit and land back on the ground at a predictable time with a predictable speed. However, at the scales of atoms, that isn't true anymore. At such scales, particles behave in a probabilistic way. If you would "throw" an atom like a ball, it could take any orbit, even highly counterintuitive ones. However, every path will have some probability associated with it. What quantum mechanics calculates, is not the path the atom will follow but the probability it will follow a given path.

The consequences of the probabilistic nature of small particles become apparent when two such particles collide. What comes out of one collision will be unpredictable. The particles may come out of the collisions unscathed but kicked out of their original course, may have lost energy converted to new particles, or different particles may come out. But for every scenario, one can calculate a kind of "probability" that it will happen.

This probability is called a cross-section. One can understand the reason for this name by comparing a collision with a game of archery. Imagine an archer shooting an arrow at a target without aiming too much. He will hit the target with a certain probability determined by the area or the cross-section of the target.

In the same way, if two particles hit each other, one can imagine that they behave like spheres with a certain cross-section. However, contrary to intuition the size of the cross-section depends on the outcome of the collision. For instance, if we collide a positron and an electron, we might be interested in an "elastic" collision (they deflect and go on their separate ways) or "annihilation" (they merge and convert into photons). The cross-sections for both types of collisions will be different. Furthermore, cross-sections in particle physics are rather small. That is why they are usually expressed in so-called "barns" (b) with $1 \text{ b} = 1 \times 10^{-28} \text{ m}^2$.

1.2.3 The standard model of particle physics

Using special relativity and quantum mechanics, one can construct a theory describing how our universe works. Experiment drives this construction, as any newly observed particle needs to fit in. Successful theories also spark new experimental searches and measurements by predicting yet unseen phenomena. Over the past decades, this interplay between experiment and theory has led to one of the

most successful theories physics has ever conceived: the standard model of particle physics, or SM.

According to this model, the world consists of the particles (and anti-particles) shown in figure 1.1. On the left, there are the fermions, divided into two classes: quarks above and leptons below. Each class has two subtypes (rows), whose electrical charges differ by one time the electron charge e . Each fermion also falls into one of three generations (the columns), with the left generation containing the lightest and the right the heaviest fermions¹ On the right of the picture, we have the force-mediating bosons mentioned earlier.

One can write down the SM with only these bosons and the fermions, but that causes a problem: to work, such a theory can only have massless particles. An elegant solution to this problem is the Brout-Englert-Higgs mechanism, which the Belgians Francois Englert and Robert Brout and independently the American Peter Higgs first discovered [29, 30]. In short, this mechanism introduces a field, called the Higgs field, that fills all of space. The massless standard model particles have to move through this field which, in a way, “obstructs” their motion. As a consequence, they acquire an effective mass. Massless particles like photons and gluons do not interact with this field and can therefore move freely at the speed of light.

The introduction of the Higgs field comes with an associated particle, the Higgs boson, which has a prominent place in the middle of figure 1.1. It is the only boson not associated with a force. It was also the last particle of the SM discovered: at the LHC in 2012 [31, 32]. Since then, scientists have been intensely studying its properties, but there has been no deviation from the SM scenario yet. That is one of the biggest reasons the SM is considered so successful.

The SM not only successfully predicted the Higgs but also many other processes with unprecedented accuracy. Nevertheless, no physicist believes the SM is complete. It does not explain some phenomena, such as gravity, dark matter and dark energy, and neutrino masses. Furthermore, there is a growing amount of experimental “tension”: observations deviating from SM predictions but are not enough to rule out the SM. Only recently, a strong deviation appeared in the mass of the W boson [33]. For all those reasons, there is still an urgent need for better experiments. Predictions need to be tested in extremer situations and with higher precision. Only this way, there is a chance we will find a theory that supersedes the SM.

¹This assertion is actually not yet established for the neutrinos. Experiments still allow for the tau neutrino to be the lightest neutrino, although they slightly favour a heavy tau neutrino [27, 28].

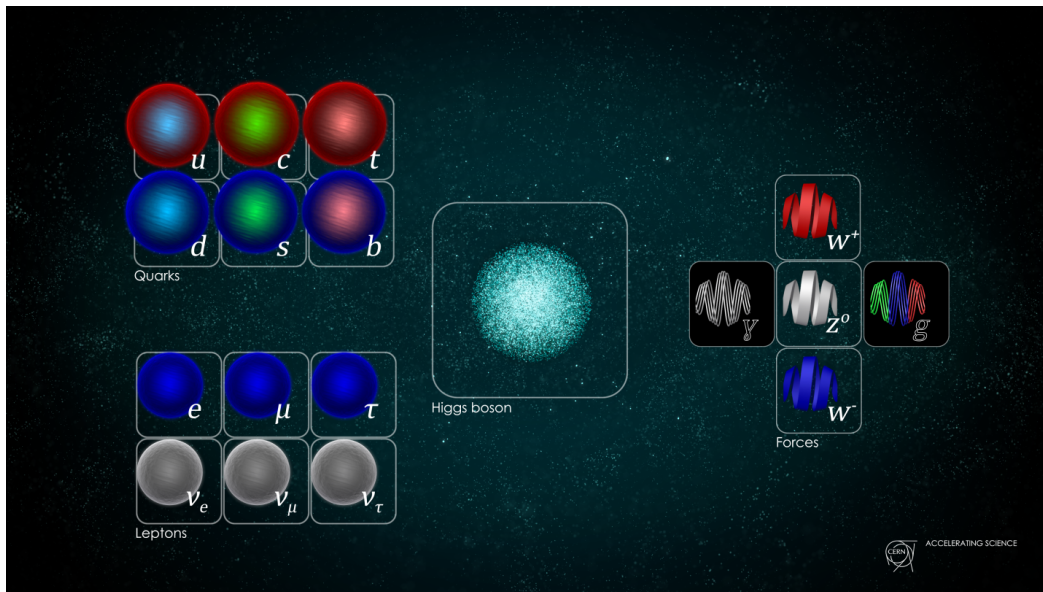


Fig. 1.1.: The particles of the standard model. Figure from [34].

1.3 Accelerators

There is a large variety of experiments one can come up with to test our current knowledge of particle physics. They can involve phenomena like radioactive decay (e.g. KATRIN [35]), antimatter energy spectra (e.g. ALPHA [36]), or cosmic gamma radiation (e.g. with the Fermi LAT [37]). Many experiments consider particle collisions of some sort. In these experiments, accelerators are omnipresent tools. These machines speed up charged particles using electrical fields up to some energy, after which they are ready to collide with some target. Accelerators can be categorised based on the kind of target, their shape, or what they accelerate.

1.3.1 The target

One possible target is a stationary object made of some dense material like lead. Experiments using such a target are called fixed-target experiments. The famous Rutherford experiment was such an experiment, although one that used a radioactive source instead of an accelerator [2]. Fixed targets often crop up in neutrino experiments, like the former OPERA experiment [38] or the future DUNE experiment [39]. The reason is that a fixed target can offer a very high collision rate because of the high density of target particles. As neutrinos interact very weakly, that is a big asset. However, the downside is that not all the energy of the incoming particle is available

for the collision. The incoming particle and the stationary target particle together have a net momentum, which must be conserved. Therefore, part of the total energy is not available for the collision.

One can overcome this problem by colliding two beams of particles moving in opposite directions. Such types of experiments are called collider experiments. The former CDF and DØ experiments that discovered the top quark were of this type [40–43]. If the beams move symmetrically, the net momentum is zero so that the full energy of both beams is available for the collision. Hence, much higher energies are attainable than in fixed-target experiments, but the collision rate will generally be lower.

1.3.2 The shape

Accelerators come into two shapes: linear and circular. As the names suggest, a linear accelerator accelerates charged particles on a straight path, while circular accelerators move the particle in a circle. One can achieve a circular orbit using magnetic fields, which bend the path of charged particles moving through them.

A linear design implies that the acceleration is a one-way trip: every particle can only be accelerated one time and, therefore, can have only one opportunity to collide. That is not the case for circular accelerators, where every particle can have many more opportunities to collide.

However, the circular movement makes it more difficult to achieve higher energies because a charged particle that accelerates will lose energy by radiating so-called synchrotron radiation [44]. This effect grows with energy but much more so for circular movement. Hence, it affects circular accelerators more than linear ones.

1.3.3 The particles

A final way to categorise accelerator experiments is according to the particles they accelerate. Although any charged particle is usable, the easiest to work with are either electrons or protons, as those are stable and abundantly available.

Leptonic accelerators use electrons, as well as positrons. The largest of this kind was the former LEP at CERN in Geneva [45]. Such an experiment has the advantage it collides fundamental particles that are simple in nature. The resulting collisions are, therefore, easier to model. Electrons are also not subject to the strong interaction,

which is usually hard to handle computationally. On the other hand, the small mass of electrons makes them much more prone to synchrotron radiation, which goes as m^{-4} [44]. Consequently, they cannot be accelerated as much.

Hadronic colliders make use of protons or sometimes heavy nuclei such as lead. Thanks to their heavy mass, such particles emit much less synchrotron radiation and can, therefore, attain higher energies. However, a proton consists of constituent particles carrying a variable fraction of the proton's energy. When colliding two high-energy protons, we actually see collisions between their constituents at a lower variable energy. That makes the situation a lot less clean and more challenging, also because the strong interaction is now directly involved. At the same time, it allows us to measure collisions at different energies simultaneously, as opposed to one well-defined energy like in the leptonic case. That is why hadronic accelerators are sometimes referred to as discovery machines. The most prominent examples are the former Tevatron (used by the DØ and CDF experiments [40, 41]) and the current LHC.

1.4 CERN and the Large Hadron Collider

The LHC, or Large Hadron Collider, is the most powerful hadronic collider built to date. It is located at CERN, an international research centre near Geneva that hosts a rich spectrum of particle physics experiments covering almost all of the categories described earlier. Figure 1.2 shows a schematic overview of all accelerator infrastructure and experiments at CERN.

The most eye-catching presence on the CERN domain are certainly the circular accelerators. They form a sequence of machines accelerating particles in a stepwise fashion. The first circular collider at CERN was the 628 m circumference Proton Synchrotron (PS) [46]. Later, it became a pre-accelerator to the larger 7 km long Super Proton Synchrotron (SPS) [47]. In 1989, CERN built an even larger ring of 27 km diameter to install a leptonic accelerator, the Large Electron Positron collider (LEP) [45]. In 2010, LEP was dismantled and replaced with the LHC.

Linear accelerators (LINACs) are used to inject particles into the accelerator chains. For instance, LINAC4 provides protons to the booster from which they continue to the PS [48]. LINAC3, on the other hand, is the starting point for heavy ions, from which they enter the Low Energy Ion Ring (LEIR) that then passes them on to the PS [49]. CERN also has a LINAC, called CLEAR (CERN Linear Electron Accelerator for Research), meant for research on accelerator technology [50].

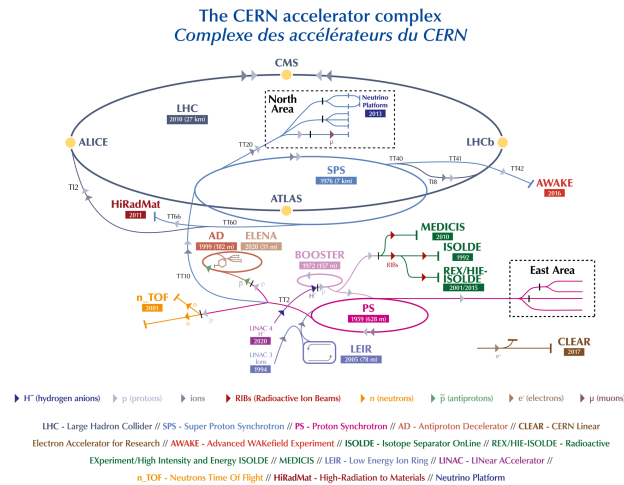


Fig. 1.2.: A schematic overview of the CERN infrastructure and experiments (not to scale). Figure from [57].

The main experiments operating on LHC are CMS (Compact Muon Solenoid) [51], ATLAS (A Toroidal LHC Apparatus) [52], ALICE (A Large Ion Collider Experiment) [53], and LHCb (with the b for beauty) [54]. All four of them are collider experiments. CMS and ATLAS are so-called general-purpose detectors, which do not target specific types of collisions. These detectors are built to detect as much as possible of the collision remnants by covering almost the entire space surrounding the collision point. ALICE, on the other hand, specialises in heavy-ion collisions, while LHCb studies mainly collisions in which the remnants are ejected almost parallel to the beamline.

Besides the collider experiments, CERN also hosts smaller fixed-target experiments. For instance, COMPASS (COMmon Muon Proton Apparatus for Structure and Spectroscopy) targets polarised protons and deuterons with muon and pion beams, which are created by hitting a target with protons from the SPS [55]. FASER (ForwArD Search ExpeRiment) has a tungsten target for studying the beams of neutrinos escaping from the collisions at the CMS collision point [56].

Large Hadron Collider

” *The only way for Humanity to push back the limit of knowledge and to make great progress is through difficult, challenging, and brave initiatives.*

— **Fabiola Gianotti**
Director General at CERN

The topic of this thesis is inextricably linked with the Large Hadron Collider (LHC) at CERN in Geneva. It is, therefore, useful to have a closer look at this particular collider. Along the way, I will introduce the theory, instrumentation and jargon that foster a better understanding of the chapters hereafter.

2.1 Overall structure

The LHC accelerates protons up to an energy of 7 TeV in two opposite directions inside a ring of 27 km circumference [6]. As one can see in figure 2.1 this ring is not a perfect circle but an alteration of eight straight sections and eight arcs. A section between two consecutive arc centres is called an octant. The arcs contain mainly dipole magnets that bend the particles on a circular orbit. Left and right to the arcs, dispersion suppressors focus the beams using a combination of dipole and quadrupole magnets. In the straight sections, the beams undergo various kinds of manipulation, such as cleaning, dumping, or colliding [58]. The actual collisions of the beams happen at four points called interaction points (IP). Here the two beams switch between the outer and inner orbit of the ring such that each beam travels the same overall distance. CMS is located at IP5, referring to the fifth straight section.

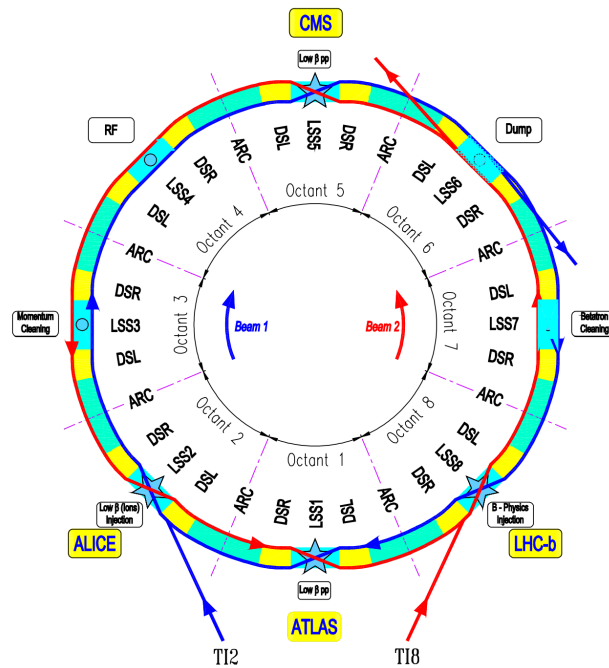


Fig. 2.1.: Schematic layout of the LHC. The ring is made of Long Straight Sections (LSS) and arcs with Dispersion Suppressors (DSL and DSR) in between. Figure from [6].

2.2 Proton bunches

The beams are no continuous streams of protons but rather a sequence of bunches. The LHC can produce a bunch every 25 ns, which divides the ring into 3600 bunch slots. However, for operational reasons, one can fill only a maximum of 2800. The bunches themselves have a width in time of 2.5 ns. This time interval divides every bunch slot into ten subintervals, called Radio Frequency (RF) buckets, of which ideally only one contains protons.

Although in principle, all charges circulating in the ring should be part of a bunch, protons can end up detached from the rest by accident. If such protons move inside nominally empty bunch slots, we refer to them as ghosts. On the other hand, satellites are part of a filled slot but move inside a nominally empty RF bucket. Both ghosts and satellites are detectable with the help of the Longitudinal Density Monitor (LDM)[59]. This detector measures the longitudinal profile of the beams (i.e. the relative proton populations along the beamline) at an even higher time resolution (50 ps). The measurement uses the synchrotron radiation that the protons emit as they move in a circular orbit.

2.3 Beam currents

An essential parameter of the LHC is the number of protons per bunch or bunch current, which is typically around 1×10^{11} . Two basic techniques to measure it are available [60], one of which uses the magnetic field induced by the beam current. As the beams are a collection of separate bunches, these magnetic fields vary in time and create currents in neighbouring conductors. A detector using this technique is called a Fast Current Transformer (FCT). Its main advantage is its high time resolution which allows it to measure the bunches separately. LHC uses FCTs with a time resolution of 25 ns, corresponding to one bunch time slot [61]. These FCTs are called FBCTs with the B for “bunch”.

An alternative is the DCCT or Direct Current Current Transformer, which figure 2.2 pictures diagrammatically. Such a detector consists of two parallel ring-shaped yokes magnetised alternately up to saturation in a symmetric fashion. I.e. the net field of both rings is zero. Around both rings, there is a coil in which the alternating magnetic fields generate currents, but no net current will flow as the fields of both rings cancel each other. If, however, a direct current flows through the ring centres, they will be magnetised preferentially in one direction. Under such circumstances, one of the rings saturates faster than the other, meaning the net field in both rings starts alternating, and the third coil sees a current.

The DCCT system used at LHC is described in [62]. It can determine the overall current (i.e. the sum of all bunches) with a precision of 0.2 %, which is much better than FBCT, which has a 1 % precision per bunch. However, as the DCCT relies on the average, direct current, it has a much worse time resolution ($20 \mu\text{s}$). Therefore, one renormalises the FBCT measurements to the measured DCCT current.

Both DCCT and FBCT measurements require some care since ghosts and satellites also contribute to the current. The FBCT cannot pick up ghosts because their charge falls below the FBCT threshold current. However, its measurement will include satellites since it measures the whole charge per bunch slot rather than per RF bucket. The DCCT adds the integrated charge of both ghosts and satellites to its measurement. Accounting for these facts, the current n^j of the j th bunch in a series of bunches is

$$n^j = n_{\text{FCT}}^j (1 - f_{\text{sat}}^j) \frac{N_{\text{DCCT}}(1 - f_g)}{\sum_k n_{\text{FCT}}^k}, \quad (2.1)$$

where f_{sat}^j is the fraction of satellites in the bunch, and f_g is the ghost fraction of all bunches together.

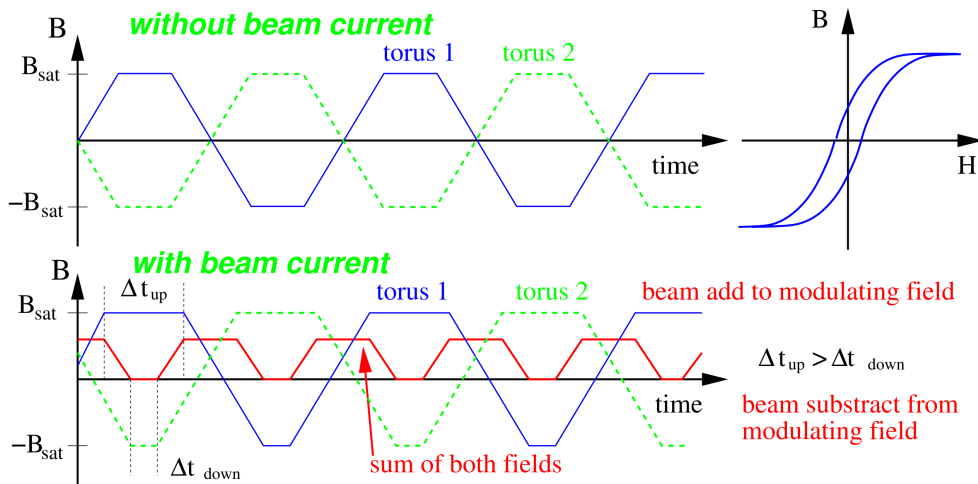


Fig. 2.2.: DCCT measurement principle. The alternating fields in both tori cancel each other, such that no current flows through a coil wrapped around both tori. A direct current breaks the symmetry, such that a net field arises and current starts flowing. Figure from [60].

2.4 Beam positions

The bunch position is a second parameter characterising the bunch as a whole. It is usually expressed in either μm or mm . Its measurement is crucial for the safe operation of the LHC, and to measure other important parameters such as luminosity and beam optics, as will be discussed later.

The basic principle of a beam position measurement is image current, which is the current induced by the passing bunches in nearby conductors [60]. These nearby conductors are the so-called pick-up plates, insulated metal plates incorporated in the the beam pipe walls. The closer the bunch passes by the pick-up plate, the stronger the resulting current. With two oppositely facing pick-up plates, one can use the difference of the currents in both plates as a position measurement. With a configuration like the one in figure 2.3, one can determine the two-dimensional position in the transverse plane.

The LHC has over a thousand BPMs, most of which are in the arcs or the dispersion suppressors [6]. The LHC also has a somewhat different type of BPM called DOROS (Diode Orbit and Oscillation system) [63]. Those use the same technique but process the signal differently from standard BPMs, using diodes to achieve a higher resolution and be sensitive to small oscillations. The LHC has DOROS systems located on its collimators and next to the interaction points at the experiments.



Fig. 2.3.: **Left:** schematic drawing of a button BPM configuration. **Right:** parts of a button BPM used at LHC. The left part is directed towards the inside of the beam tube. Images from [60].

2.5 Beam optics

Making a proton move in a circular orbit requires a centripetal force, i.e. a force that is always at right angles with the movement. Such a force is precisely what uniform magnetic fields generate. Indeed, a particle of charge q moving at a speed \vec{v} inside a constant field \vec{B} will be subject to the Lorentz force

$$\vec{F} = q\vec{v} \times \vec{B}.$$

One can achieve a uniform magnetic field with two flat magnets with a south (S) and north (N) pole by positioning the S pole of one magnet parallel to the N pole of the other. Such a construction is called a dipole magnet.

In the LHC, not just one proton is in orbit, but a whole bunch. Inevitably, the protons within such a bunch repel each other. Furthermore, in the straight section, the protons do not feel the dipole field anymore, and tend to move away from the central orbit anyway. There is, therefore, a need to focus the beams, which is a job reserved for the quadrupole magnets. As the name suggests, such a magnet is made of four poles arranged as on the left in figure 2.4. A particle moving away from the reader inside the field of figure 2.4 will experience a vertical force towards and a horizontal force away from the centre. With a construction like on the right in figure 2.4, one can achieve the desired focussing.

The entire magnetic layout of the LHC is referred to as beam optics. Besides dipoles and quadrupoles, it also contains higher-order multipole magnets with different purposes. An exact calculation of the beam dynamics is impossible. However, for the case of the LHC, the Hill's equations provide a good approximation for small perturbation around the stable orbit [66]:

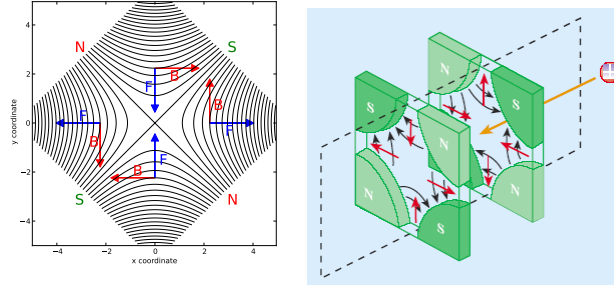


Fig. 2.4.: **Left:** Field lines of an ideal quadrupole magnet. The forces (blue) are shown for a particle moving away from the reader. Figure from [64]. **Right:** Focusing combination of quadrupoles. Figure from [65].

$$x''(s) + \left(\frac{1}{\rho_n^2(s)} + K_n(s) \right) x(s) = 0 \quad (2.2)$$

$$y''(s) - K_n(s)y(s) = 0 \quad (2.3)$$

where s is the coordinate along the beamline, x the coordinate along the orbit's radius, and y the coordinate perpendicular to the orbit's plane. ρ_n is the radius of the orbit determined by the dipolar magnets, while K_n is the quadrupole focussing strength. Note that the quadrupole effect comes with a different sign in both equation, indicating that a single quadrupole focussing in one plane will defocus in the other.

Equations (2.2) and (2.3) are reminiscent of classical harmonic motion with force constant $K_x = 1/\rho_n^2 + K_n$ or $K_y = -K_n$. If the $\rho_n(s)$ and $K_n(s)$ vary slowly with s , then that is locally true. Therefore, the solution is harmonic with an s -dependent frequency and amplitude [67]:

$$u(s) = \sqrt{\epsilon\beta(s)} \cos(\phi(s) - \phi)$$

with $u = x, y$. Note that the functions and constants to the left are different for $u = x, y$.

The *emittance* ϵ is a length scale describing the overall amplitude of the oscillation. In principle, every particle has a different emittance, but one can take the root mean square $\epsilon_{u,\text{rms}}$, for instance, to define a bunch emittance.

The *beta function* $\beta(s)$ only depends on the magnetic structure, as it obeys

$$\frac{1}{2}\beta'\beta - \frac{1}{4}\beta'' + \beta^2 K_u = 1$$

which follows from resubstituting the solution into Hill's equations. This function is, therefore, the same for all particles. Together with the bunch emittance, it defines the *beam envelope* $\sqrt{\epsilon\beta(s)}$.

Finally, the function $\phi(s)$ is called the *phase advance*. It is directly related to the beta function via

$$\phi(s) = \int_0^s \frac{ds}{\beta(s)}$$

which also follows from resubstitution. From the phase advance one can derive the *tune* as the phase advance over one full orbit divided by 2π :

$$Q = \frac{1}{2\pi} \oint \frac{ds}{\beta(s)}.$$

It represents the number of oscillations the particle executed over the distance s .

An alternative form for the solution to Hill's equations is the *transfer matrix* M . Given the position u and angle u' at $s = 0$, one can compute (u, u') at any s via

$$\underbrace{\begin{pmatrix} \sqrt{\frac{\beta}{\beta_0}} (\cos \phi + \alpha_0 \sin \phi) & \sqrt{\beta\beta_0} \sin \phi \\ \frac{\alpha_0 - \alpha}{\sqrt{\beta\beta_0}} \cos \phi - \frac{1 + \alpha_0\alpha}{\sqrt{\beta\beta_0}} \sin \phi & \sqrt{\frac{\beta}{\beta_0}} (\cos \phi - \alpha_0 \sin \phi) \end{pmatrix}}_{M(s)} \begin{pmatrix} u \\ u' \end{pmatrix}_0 \quad (2.4)$$

where $\alpha = -\beta'/2$ measures the slope of the beta function. When one wants to compute the propagation of the protons from one collision at an IP to the next, one can use a simplified formula because the beta function reaches a minimal value, β^* , at the IPs. One wants, after all, to maximise collision rates, hence make the beam size as small as possible. That means $\alpha_{\text{IP}} = 0$, so the transfer matrix of a full turn, in this case, becomes

$$\begin{pmatrix} u \\ u' \end{pmatrix}_0 \mapsto \underbrace{\begin{pmatrix} \cos 2\pi Q & \beta^* \sin 2\pi Q \\ -\frac{1}{\beta^*} \sin 2\pi Q & \cos 2\pi Q \end{pmatrix}}_{M^*} \begin{pmatrix} u \\ u' \end{pmatrix}_0 \quad (2.5)$$

The beam optics parameters strongly influence the performance of the LHC, so their measurement is an important task. For the emittances, several methods are available [68, 69]. The reference method at the LHC is the wire scanners. These devices move a thin carbon wire across the beam and measure the radiation which the interaction between the wire and the protons induces. Another method is based on synchrotron radiation. This transverse analogon to the LDM is called the Beam Synchrotron Radiation Telescope (BSRT). It is calibrated using the wire scanners. The overall accuracy of the emittance measurements is in the range of 10 % to 20 %.

Measuring the phase advance and tune amounts to counting the number of oscillations after applying a kick to the beam away from the stable orbit [70]. The BPM measurements are essential for this counting, especially those of DOROS. That system can measure oscillations of smaller amplitude than normal BPMs can, such that a smaller and safer kick suffices.

Two methods are available for a beta function measurement: the wire scanners or K -modulation [71, 72]. In the latter method, one changes the strength of a quadrupole by an amount ΔK , resulting in a shift $\Delta\phi$ in the measured tune. Then if the shift is small, one can show that $\beta_{x,y} = \pm 4\pi\Delta\phi/\Delta K$. The sign is different for the x and y planes since a quadrupole magnet defocusses in one plane and focusses in the other. A typical uncertainty for this method is 2% to 5%, which is much smaller than the 10% to 20% uncertainty range of wire scanners.

Luminosity

” *And God said, Let there be light: and there was light. And God saw the light, that it was good: and God divided the light from the darkness.*

— **King James Bible, Gen. 1. 3-4**

The name luminosity derives from the Latin word *lumen*, which means light. That makes the name somewhat confusing, as we are not dealing with photons but with accelerated protons or electrons. The fact that luminosity in astronomy already denotes the total energy output per second of a star only adds insult to injury. However, the following will show that, in some sense, the different meanings of luminosity do not differ that much.

3.1 What is luminosity

In the head of a particle physicist, the luminosity of a collision experiment is the number of times one tries to generate a collision every second. This intuition arises because of the analogy with a game of dice throwing. As explained in chapter 1, one collision represents a purely random process with an associated cross-section depending on the outcome of the collision. One can think of a collision as one throw with an unknown die, with every dice number representing a possible outcome of the collision.

A scientist wants to investigate the die but cannot look at it directly. He can, however, throw it as many times as he wants and know the numbers he threw. Then imagine the scientist counts twelve fives. This fact alone is already a discovery in its own right since our investigator now knows there is a five written on the dice. However, the probability p of throwing a five could still be anywhere between 0% and 100%. To get an idea of p , the investigator had to count the number of throws N , so he would know the probability is approximately $12/N$.

A collision experiment is essentially the same as the dice research of our investigator. We take a hypothetical type of collision and count the average number of times dN

we observe it per time interval dt . If we find a non-zero dN , we have discovered that the collision exists. Then we want to compute the cross-section σ . To do so, we use

$$\frac{dN}{dt} = \sigma \mathcal{L}, \quad (3.1)$$

where \mathcal{L} is called the *instantaneous luminosity*. A typical unit is $\text{cm}^{-2} \text{s}^{-1}$. As already mentioned, it represents the number of attempts to create the given collision. Of course, we cannot count collisions instantaneously (i.e. with δt infinitely small). Usually, we count the number of collisions over an extended time, which amounts to integrating equation (3.1). In that time, \mathcal{L} can change, but σ is constant. Hence, the following formula

$$N = \sigma \int \mathcal{L}(t) dt \quad (3.2)$$

We talk now about the *integrated luminosity* $\int \mathcal{L} dt$, which is usually expressed in fb^{-1} . (Recall that $1 \text{ b} = 1 \times 10^{-28} \text{ m}^2$.) Particle physicists usually report this number when asked about the data amount their experiment has amassed.

Although one can liken luminosity to dice throwing, there is a crucial difference which one can understand by looking at figure 3.1. It shows a collision of two bunches counting N_1 and N_2 protons, respectively, which is repeated at a frequency ν . Thinking about the luminosity as the number of collision attempts, one could say that every pair of protons, $N_1 N_2$ in total, represents one attempt. So we have $\nu N_1 N_2$ attempts every second, or $\mathcal{L} = \nu N_1 N_2$. However, this reasoning overlooks one factor: the area over which the protons spread out. If that area is large, only a few protons will collide, while if it is small, more collisions will happen. This area, called the transverse luminous area, is under our control, so it must also be a part of the number of collision attempts. Hence, one can calculate luminosity as

$$\mathcal{L} = \frac{\nu N_1 N_2}{A_{\text{lum}}} \quad (3.3)$$

3.2 Why luminosity matters

When learning about luminosity, it is easy consider it only a minor issue compared to “really” matters, i.e. the cross-sections. Indeed, knowledge of the luminosity value does not tell you any secrets about the essence of Nature. It only quantifies the power of the experiment at hand. Nevertheless, it is crucial knowledge.

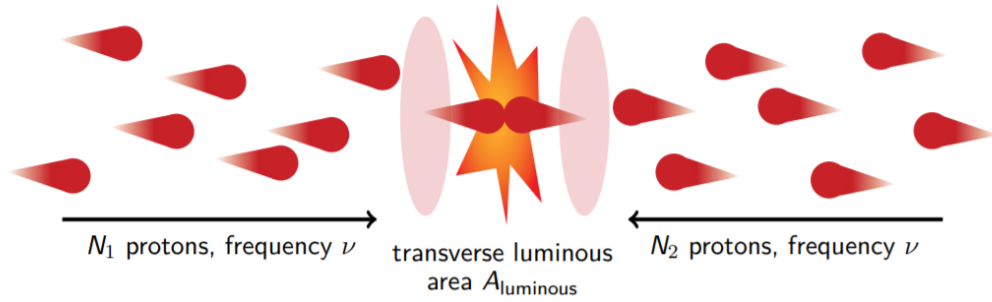


Fig. 3.1.: An illustration of luminosity for two colliding proton bunches. Figure from [73]

Equations (3.1) and (3.2) tell that calculating cross-sections amounts to counting collisions and dividing the observed number through the luminosity. So, first of all, without the luminosity, one cannot determine cross-sections directly. Moreover, any uncertainty on \mathcal{L} directly affects all cross-section measurements in the same way. That is not a problem if the uncertainty on N dominates, but as we collect more data and improve reconstruction techniques, N becomes ever more precise. For this reason, the luminosity uncertainty has started to dominate the overall uncertainty in some measurements.

For instance, luminosity alone accounts for 19% of the total uncertainty on the latest inclusive cross-section measurement for top quark-antiquark pair production with emission of a photon [19]. For the CMS measurement of WZ production, the luminosity contribution is even 28% [20]. Even in differential cross-sections, the luminosity uncertainty can dominate, which is the case in the latest CMS measurement of Drell-Yan pair production (which is not published yet) [21]. Drell-Yan pairs are lepton-antilepton pairs arising from a virtual photon. Figure 3.2 shows uncertainty on the measured cross-section of this process as a function of the transverse momentum of the Drell-Yan pair.

3.3 Theory of luminosity

Given the importance of luminosity, it is worthwhile to look more closely at it. Equation (3.3) already gives us insight into what factors influence the luminosity but does not tell us what A_{lum} exactly represents. To know more, we will make use of the archery analogy.

Imagine an archery game in which we have N_t targets of cross-section σ suspended in a room, open one side with area A . The vision of an archer looking at the room

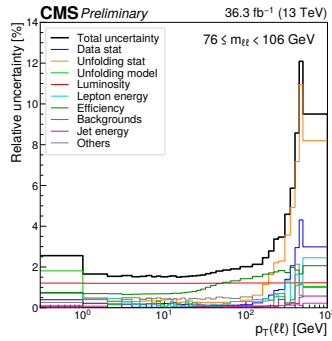


Fig. 3.2.: Relative uncertainty on the Drell-Yan pair production cross-section with an invariant mass in the range 76 GeV to 106 GeV as a function of the transverse momentum of the Drell-Yan pair. Luminosity accounts almost exclusively for the error on the central bins. Figure from [21].

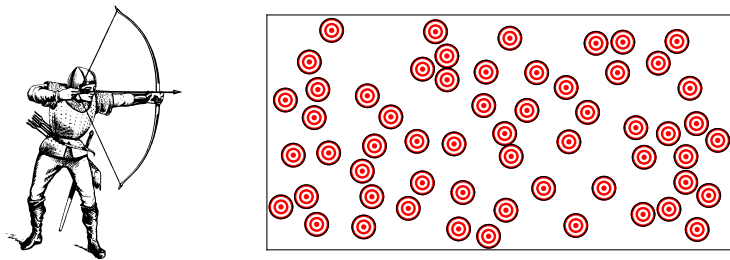


Fig. 3.3.: Vision of the archer on the targets. The total area A is covered by N targets of cross-section σ . The hit probability is $N\sigma/A$.

would look like the right side of figure 3.3. If he shoots an arrow at random within the boundaries of the open wall, the chance of hitting a target will be $p = N_t\sigma/A$.

Now imagine the room extends infinitely far in the direction perpendicular to the open wall, with a uniform target density n_t throughout. Then the targets will cover the entire vision of the archer so that always $p = 1$. That is not very interesting, so instead, we look at the probability the arrow will hit a target within a time interval Δt . If the arrow moves at a speed v , it will have covered a distance $v\Delta t$ barring the possibility it hits something. The number of targets it can potentially hit in that time is thus within the volume $Av\Delta t$ and equal to $N_t = n_tAv\Delta t$. Now we are back in the finite room situation so that the hit probability within the time Δt is $p = N_t\sigma/A = n_tv\sigma\Delta t$.

As a next step, we consider the case where we have not just one archer shooting one arrow but a whole group of archers shooting a cloud of arrows. Assume the cloud extends uniformly with density n_a over a length d within the room and moves at a speed v . Then we have $N_a = n_ad$ arrows, each with a hit probability $p = n_tv\sigma\Delta t$

within the time Δt . We expect, therefore, $\Delta N = N_a p = n_a A d n_t v \sigma \Delta t$ events per time Δt . According to formula equation (3.1), the instantaneous luminosity is

$$\mathcal{L} = \frac{1}{\sigma} \lim_{\Delta t \rightarrow 0} \frac{\Delta N}{\Delta t} = n_a A d n_t v.$$

The archery situation described is the analogy for a cuboid uniform particle cloud of length d and cross-section A moving through a rectangular tube of the same cross-section uniformly filled with particles. And although real-life particles do not have a target-like cross-section, the same formula still applies.

The above situation with a cuboid moving through a rectangular tube is somewhat artificial. In reality, one has two particle clouds, C_1 and C_2 , moving with speeds \vec{v}_1 and \vec{v}_2 , whose densities $n_1(\vec{r}, t)$ and $n_2(\vec{r}, t)$ vary. Assume for a moment the clouds move along the same line. Then we can simplify the situation by putting ourselves in a reference frame fixed to C_2 where C_1 moves with speed $|v_1 - v_2|$ along, say, the z -axis. Then at a time t , we can consider a small cuboid of C_1 centred on the point \vec{r} of length dz along the z -axis, cross-section dA , and volume $dV = dz dA$. If the cuboid is very small, and the densities of C_1 and C_2 vary smoothly in space and time, then both n_1 and n_2 can be considered locally constant. Hence, the local instantaneous luminosity is

$$d\mathcal{L}(\vec{r}, t) = |v_1 - v_2| n_1(\vec{r}, t) n_2(\vec{r}, t) dV.$$

Now we add all local contributions to the total instantaneous luminosity of all possible cuboids:

$$\mathcal{L}(t) = |v_1 - v_2| \int dV n_1(\vec{r}, t) n_2(\vec{r}, t).$$

At the LHC, this instantaneous luminosity is not that interesting. More interesting is the *luminosity per bunch crossing*, which is the integrated luminosity for the time over which two bunches cross each other. For the two bunches, C_1 and C_2 , it would equal

$$\mathcal{L} = |v_1 - v_2| \int_{-\infty}^{\infty} dt \int dV n_1(\vec{r}, t) n_2(\vec{r}, t).$$

Furthermore, the LHC accelerates bunches to high speed so that during the crossing, the bunches don't change their shape. That means $n_i(\vec{r}, t) = n_i(\vec{x}, z - v_i t)$ for $i = 1, 2$ with $\vec{x} = (x, y)$ the position in the transverse plane. Then

$$\mathcal{L} = |v_1 - v_2| \int d\vec{x} \int_{-\infty}^{\infty} dt \int_{-\infty}^{\infty} dz n_1(\vec{x}, z - v_1 t) n_2(\vec{x}, z - v_2 t).$$

We can apply a change of variables $(t, z) \mapsto (u_1 = z - v_1 t, u_2 = z - v_2 t)$ with $du_1 du_2 = |v_1 - v_2| dz dt$ and define the transverse densities $\tilde{n}_i(\vec{x}) = \int_{-\infty}^{\infty} du_i n_i(\vec{x}, u_i)$ for $i = 1, 2$. Then the per-bunch luminosity is

$$\mathcal{L} = \int d\vec{x} \tilde{n}_1(\vec{x}) \tilde{n}_2(\vec{x}).$$

To retrieve formula equation (3.3), we rewrite the transverse densities as the particle number times the density profile $\tilde{n}_i(\vec{x}) = N_i f_i(\vec{x})$. The density profile is normalised to unity: $\int d\vec{x} f_i(\vec{x}) = 1$. Furthermore, we assume we have ν crossings per unit of time. Then the luminosity per unit of time is

$$\mathcal{L} = \nu N_1 N_2 \int d\vec{x} f_1(\vec{x}) f_2(\vec{x}). \quad (3.4)$$

From this we see that

$$A_{\text{luminous}} = \left(\int d\vec{x} f_1(\vec{x}) f_2(\vec{x}) \right)^{-1}, \quad (3.5)$$

which concludes the derivation.

3.4 Measurement

With the precise meaning of luminosity at our disposal, we can now discuss ways to measure it. There are several possibilities, all of which have their advantages and disadvantages.

3.4.1 From machine parameters

The most obvious method is applying equation (3.4) directly. As discussed in section 2.3, one can make direct measurements to determine the currents N_1 and N_2 as in equation (2.1). Any device whose time resolution is small enough to discern different bunches, like the FBCT, can measure the frequency. The luminous area is a bit trickier, but by making reasonable assumptions on the bunch density profile, e.g. that it is gaussian, the integral has an analytical solution. To calculate A_{lum} , one only needs to measure the beta function and bunch emittance at the interaction point. However, as mentioned in section 2.5, the uncertainty of the emittance measurement can be over 10% and is at best a few per cent if measured using K-modulation.

If we want a better precision for the luminosity, we need to resort to a different approach.

3.4.2 From a known cross-section

As equation (3.4) did not yield a satisfactory precision, one can try using the other defining relation of luminosity: equation (3.1). If one has a process available with a cross-section known with sufficiently high accuracy, one can count how many times one observes that process and divide by the cross-section.

LEP, the leptonic collider preceding LHC, used this procedure based on elastic electron-positron scattering or Bhabha scattering. Because this is an electromagnetic process between two fundamental particles, one can make precise calculations. Moreover, this process has a large cross-section so that one quickly achieves high statistics with a correspondingly small statistical uncertainty. That is why LEP could achieve an impressive uncertainty as small as 0.05 % [74].

At LHC, however, there is no process as ideal as Bhabha scattering. Since it is a hadronic collider, almost all calculations involve QCD calculations which are much less tractable. Any computation must also account for the inner structure of the proton, which we only know through experimental research. That alone already induces an uncertainty of about 2 % to 3 %. (See e.g. [20, 75].) Moreover, if one chooses a less QCD-prone process, one quickly finds oneself with too low statistics.

3.4.3 The Van Der Meer Method

The previous two options are straightforward, but do not work for the LHC. Still, it is possible to arrive at per cent level precision using equation (3.4) cleverly. The idea is to displace one of the beams in the transverse plane over a vector $\vec{\delta} = (\delta_x, \delta_y)$. We can make this displacement apparent in equation (3.4) like this:

$$\mathcal{L}(\vec{\delta}) = \nu N_1 N_2 \int d\vec{x} f_1(\vec{x}) f_2(\vec{x} + \vec{\delta}).$$

The luminosity is now a function of $\vec{\delta}$, which we can integrate:

$$\int \mathcal{L}(\vec{\delta}) d\vec{\delta} = \nu N_1 N_2 \int d\vec{\delta} \int d\vec{x} f_1(\vec{x}) f_2(\vec{x} + \vec{\delta}).$$

By the change of variable $\vec{x}' = \vec{x} + \vec{\delta}$, the second integral factorises like

$$\int \mathcal{L}(\vec{\delta}) d\vec{\delta} = \nu N_1 N_2 \int d\vec{x} f_1(\vec{x}) \int d\vec{x}' f_2(\vec{x}') = \nu N_1 N_2,$$

where we used that the profile density functions are normalised to unity. One can now choose a reference process with an unknown cross-section σ_{vis} , (referred to as the visible cross-section). Applying equation (3.1) we find:

$$\sigma_{\text{vis}} = (\nu N_1 N_2)^{-1} \int \frac{dN}{dt}(\vec{\delta}) d\vec{\delta}. \quad (3.6)$$

The integral on the righthand side is measurable by counting the number of processes at different $\vec{\delta}$ and taking the sum. We already know how to measure the currents and the frequency. Hence, with this equation, one can determine σ_{vis} without prior knowledge of the luminosity. Moreover, we only have to do this entire procedure once as the cross-section is, in principle, a constant, and from then on, proceed like in section 3.4.2.

The Van De Meer method enabled the LHC experiments to reach a precision around the 2% level [13, 15]. Getting to such precision is far from trivial and requires an extensive study of all the assumptions and corrections needed to compute equation (3.6) correctly. The next chapter will discuss this in more detail.

The Van Der Meer Method

” Je moet open staan om warrige, rare ideeën uit te werken. Als je denkt: dat is krankzinnig, dat ziet iedere gek, dan moet je het juist niet aan de kant schuiven.

— **Simon Van Der Meer**

Dutch accelerator physicist at CERN

Superficially, the Van Der Meer (VdM) method is simple. However, every step in this procedure requires various assumptions to make the theory practicable. These assumptions only hold to a certain extent, and their application introduces errors in the final result. Therefore, one must apply corrections to get a high-precision measurement. The following paragraphs will describe the VdM procedure, which assumptions it makes, and how to mitigate the errors induced by those assumptions. The discussion will be from the CMS viewpoint, as expounded at length in [15–17].

4.1 Luminometers

The first step of the VdM procedures covers the choice of the process which will be measured, as well as the detector that will perform the measurement. The chosen detector is then a *luminometer*, while the process's cross-section is the visible cross-section σ_{vis} . The measurement of σ_{vis} takes place during a specialised time slot called the *VdM calibration fill*.

Apart from measurements of the currents equation (3.6) entirely relies on the luminometers themselves. Consequently, σ_{vis} is not just the cross-section of an abstract process: it is the cross-section for measuring the process with the given luminometer. That means that σ_{vis} is dependent on the detector itself, which violates two key assumptions of equation (3.1): *stability* and *linearity*.

Stability means that the cross-section does not change over time. For a physics process, this assumption is almost trivial, provided the laws of physics do not change.

But a detector can degrade in performance over time because of radiation damage inflicted by the intense collision rate of LHC. As the detector degrades, σ_{vis} will change because, for instance, the chance of measuring the process becomes smaller or the background increases.

Linearity means that σ_{vis} is independent of luminosity or that this equation is linear in \mathcal{L} . Again, this assumption is trivial for a physics process but not for a detector process. Detectors will much more easily detect a given event if it has to deal with only a few events simultaneously. The more is going on, the higher the chance that two events create a coincident signal in time and place, which the detector counts as one. For this reason, detectors will consistently undercount the total number of events, and the higher the event rate, the more severe this undercounting becomes.

A problem related to non-linearity is out-of-time pile-up, which occurs when bunch crossings happen at a high frequency. In such circumstances, the detection of events during one crossing can influence the detection during the next crossing because the detector requires a non-zero time to record and recover from an event. That needs to be accounted for when using a given luminometer.

4.2 The VdM integral

Once the luminometer and associated process are determined, one needs to calibrate it, i.e. measure σ_{vis} . That involves the computation of equation (3.5), which requires measurements over all possible displacements in the 2D plane. Such a series of measurements is called a *scan*. Of course, a scan can only contain a finite amount of measurements, so the integral has to be approximated as a discrete sum. But such approximation leads to large statistical uncertainties.

A better approximation takes into account that beam profiles are smooth function so that the observed event rate varies smoothly with the event rate. For instance, one can use a Gaussian profile:

$$f_i(\vec{x}) = \frac{1}{2\pi\sqrt{\det V_i}} \exp\left(-\frac{1}{2}\vec{x} \cdot V_i \cdot \vec{x}\right),$$

with V the 2D covariance matrix. Using standard Gaussian integral identities, this results in

$$\frac{dN}{dt}(\vec{\delta}) = \sigma_{\text{vis}}\mathcal{L}(\vec{\delta}) = \frac{\sigma_{\text{vis}}\nu N_1 N_2}{2\pi\sqrt{\det V}} \exp\left(-\frac{1}{2}\vec{\delta} \cdot V \cdot \vec{\delta}\right),$$

with $V = V_1 + V_2$ the convoluted covariance matrix. One can find V by fitting a Gaussian function to the observed rates at different displacements from which we calculate $A_{\text{lum}} = 2\pi\sqrt{\det V}$ and, ultimately, σ_{vis} .

Another feature of the Gaussian approach is that one only needs two one-dimensional scans to make the fit work. Indeed, we can align our frame of reference with the eigenbasis of V , such that $V = \text{diag}(\Sigma_x^2, \Sigma_y^2)$. Then

$$\frac{dN}{dt}(\vec{\delta}) = \frac{\sigma_{\text{vis}}\nu N_1 N_2}{2\pi\Sigma_x\Sigma_y} \exp\left(-\frac{\delta_x^2}{2\Sigma_x^2} - \frac{\delta_y^2}{2\Sigma_y^2}\right). \quad (4.1)$$

Then the scans along the lines $\delta_x = 0$ and $\delta_y = 0$ yield Gaussian profiles with widths Σ_y and Σ_x , respectively. One then fits a Gaussian to both scans independently and computes $A_{\text{lum}} = 2\pi\Sigma_x\Sigma_y$.

The problem is that the eigenbasis of V is not known a priori, so it is not clear in which directions the scans have to be. However, to a good approximation, the eigenbasis of V coincides with the LHC coordinate frame. So usually, it is assumed that V is fully diagonal, and one performs the scans along the X - and Y -axis of the LHC frame of reference. More generally, this assumption relies on *factorizability*: the two-dimensional event rate factorizes into two one-dimensional functions of x and y . In case V is not diagonal, one finds that the widths of the profiles in both scans diminish by a factor $\sqrt{1 - \rho^2}$ with ρ the correlation coefficient. Hence, assuming factorizability results in a systematic underestimation of A_{lum} , called factorization bias.

Another problem is that the bunch widths encoded in V_1 and V_2 should a priori depend to some extent on the displacement $\vec{\delta}$. This dependency occurs because the protons of both bunches repel each other, which causes a widening of the bunch widths. We call this phenomenon incoherent beam-beam interaction because it results from the interaction of individual protons rather than bunches as a coherent whole. The effect on the luminosity is complex and, therefore, estimated numerically using Monte Carlo simulation [76].

4.3 Displacing the beams

After deciding how to calculate the luminous area, one needs to figure out how to displace the beams. The displacement of one beam in a fixed direction requires a pair of corrector magnets: one kicks the bunch off course while the other relevels the bunch. On the other side of the IP, two corrector magnets perform the same

action in reverse. The goal is to create *closed orbit bumps*: the beams are displaced inside the corrector magnet region, but their orbit outside that region should be undisturbed. In total, for two beams and two directions, there are sixteen magnets active in this manoeuvre located between 160 m and 230 m from the IP.

The corrected magnets get instructions to displace the beams to a so-called *nominal* position, but the effective position after displacement will deviate slightly. Several effects can or could result in such deviations.

4.3.1 Length scale and misalignment

First of all, the response of the magnets will generally not exactly correspond to the nominally required response. In general, the response to a nominal displacement $(x_{\text{nom}}, y_{\text{nom}})$ is given by

$$\begin{pmatrix} x \\ y \end{pmatrix} = \begin{pmatrix} \alpha_x & \beta_x \\ \beta_y & \alpha_y \end{pmatrix} \begin{pmatrix} x_{\text{nom}} \\ y_{\text{nom}} \end{pmatrix}, \quad (4.2)$$

where $\alpha_{x,y} \approx 1$ are the *length scale* factors and $\beta_{x,y} \approx 0$ the *misalignment* factors. Usually, one assumes a linear response, which means neither α nor β depends on the displacement.

Non-unity length scale factors imply that the scale of the magnet response is not exactly equal to the nominal scale. Non-zero misalignment factors tell us that the frame of reference of the magnets is slightly tilted relative to the nominal frame.

Applying equation (4.2) to equation (4.1), we can see that a scan along the X -axis ($y_{\text{nom}} = 0$) yields a profile with width

$$\Sigma'_x = \frac{\Sigma_x}{\alpha_x} \left(1 + \frac{\beta_y^2 \Sigma_x^2}{\alpha_x^2 \Sigma_y^2} \right)^{-1/2}.$$

So the measured width scales as α_x^{-1} . Therefore, if there is any uncertainty on α_x , it will translate directly to an uncertainty A_{lum} and σ_{vis} . The misalignment, on the other hand, introduces a bias similar to the factorization bias with $\rho = \beta_y \Sigma_x / \alpha_x \Sigma_y$.

4.3.2 Coherent beam-beam effects

We already encountered the incoherent beam-beam effects, which considered the repulsion between the protons of different beams individually. But the bunches as a whole also exert an electromagnetic force on each other, which results in a coherent

beam-beam effect, also called beam-beam deflection [77, 78]. Due to this force, the bunches will be deflected over an angle θ , called a *kick*. Assuming the bunches are factorizable, spherically symmetric, and rigid, this kick looks like

$$\theta_1 = \frac{\sqrt{\pi} N_2 r_p}{\gamma \Delta} \left(1 - \exp\left(-\frac{\Delta^2}{2\Sigma^2}\right) \right). \quad (4.3)$$

Here, θ_1 is the angle over which one bunch is deflected due to the force of the other bunch. The bunches are at a distance Δ from each other and have a convoluted width given by Σ . Finally, N_2 is the number of protons in the bunch exerting the force, γ is the relativistic gamma factor, and r_p is the proton radius.

We see that $\theta_1 = 0$ at $\Delta = 0$, as then the beams do not exert a net force onto each other. θ_1 also falls off again at larger Δ , as then the force gets smaller. In between, it reaches a maximal deflection. (See figure 4.1). This behaviour remains for non-symmetrical bunches, although the formulas are more complex in this case [79].

One single deflection will not lead to a measurable displacement at the collision point itself, as the collision happens too fast for that to occur. However, as LHC is circular, the bunches will deflect each other repeatedly, eventually resulting in a net displacement. To calculate it, we use the formalism from section 2.5. Suppose we move the beams to a separation Δ along the X -axis. A deviation u of beam 1 relative to its stable orbit will be described by equation (2.5). Note that the derivative u' relative to the coordinate s represents the orbit angle in the xs -plane along the beamline. Hence, the beam-beam kick can be represented by

$$\begin{pmatrix} u \\ u' \end{pmatrix}_{\text{after},0} = \begin{pmatrix} u \\ u' \end{pmatrix}_{\text{before},0} + \begin{pmatrix} 0 \\ \theta \end{pmatrix}.$$

After the kick, the beam will perform betatron oscillations while travelling through the LHC. Before colliding once more, the deviation u and angle u' are

$$\begin{pmatrix} u \\ u' \end{pmatrix}_{\text{before},1} = M^* \begin{pmatrix} u \\ u' \end{pmatrix}_{\text{after},0} = M^* \begin{pmatrix} u \\ u' \end{pmatrix}_{\text{before},0} + M^* \begin{pmatrix} 0 \\ \theta \end{pmatrix}.$$

So generally, the beam will enter the second collision at a different deviation and angle. However, there is one stable solution for the above equation, for which the deviation and angle before colliding are always the same. It is given by

$$\begin{pmatrix} u^* \\ u'^* \end{pmatrix}_{\text{before}} = (1 - M^*)^{-1} M^* \begin{pmatrix} 0 \\ \theta_1 \end{pmatrix} = \begin{pmatrix} \beta^* \cot \pi Q \\ -1 \end{pmatrix} \frac{\theta}{2}. \quad (4.4)$$

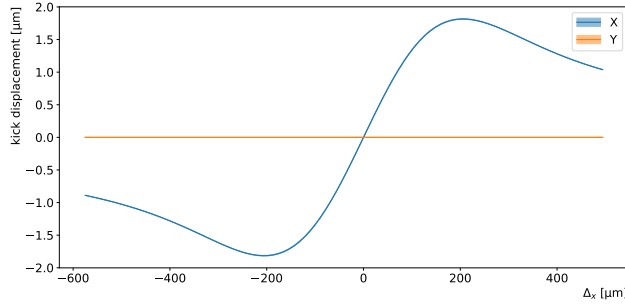


Fig. 4.1.: Displacement caused by coherent beam-beam interaction as a function of the displacement along the X -axis. The bunches are assumed to be factorizable.

Unsurprisingly, the stable orbit is one in which the beam enters and leaves symmetrically, at an angle $\theta/2$. The stable orbit with kick is displaced relative to the stable orbit without, by an amount

$$\Delta u_{\text{BB}} = \frac{\beta^* \cot \pi Q}{2} \frac{\sqrt{\pi} N_2 r_p}{\gamma \Delta} \left(1 - \exp\left(-\frac{\Delta^2}{2\Sigma^2}\right) \right) \quad (4.5)$$

Eventually, the beams will reach this new stable orbit because of friction-like effects such as synchrotron radiation. Therefore, equation (4.5) effectively gives the effect of the beam-beam deflection on the beam position.

4.3.3 Unexplained deviations

After accounting for all the previous effects, there will still be some residual deviations left. These residuals are a consequence of random changes in the LHC conditions to at least some degree. They are, therefore, not reproducible between repeated scans. One can partially correct this random constituent called *orbit drift* by comparing the (nominal) head-on positions of the beams before and after each (sub)scan.

However, that still leaves some residual differences. It is at the moment not clear what those represent. It could be fast orbit drift or a systematic effect that we have not considered before. For instance, there are some indications that the magnets suffer from hysteresis effects [80]. This phenomenon makes the magnetisation of a magnet dependent on its history, which would mean that the current beam position also would depend on the movement history of the beam.

4.4 The VdM fill

With all the above approximations and caveats in mind, one can construct a program to perform the σ_{vis} measurement. Such a program takes place every year during one dedicated *fill*, which is a period over which there is a continuous circulation of proton bunches in the LHC. From a general scientific point of view, the most interesting fills are physics fills. Their main characteristics are concentrated bunches colliding head-on at the highest possible frequency for maximal luminosity.

The VdM fill, on the other hand, uses only a limited amount of bunches coming in at a much lower frequency. That makes the interaction between subsequent bunches minimal and avoids out-of-time pile-up. The bunches are also wide to limit the number of events per crossing so that linearity issues are irrelevant. Wide bunches also make the number of events drop less fast when the beams move away from each other in the VdM scans. That allows for larger displacements, which benefits the analysis.

The defining characteristic of the VdM fill is, however, the intricate sequence of displacements as illustrated in figure 4.2. It shows the nominal beam movement during the VdM fill from 2017 at the CMS experiment. One can see several different scan types serving various purposes. The following paragraphs will describe each of them, explain their goals and how they reach them in the CMS experiment.

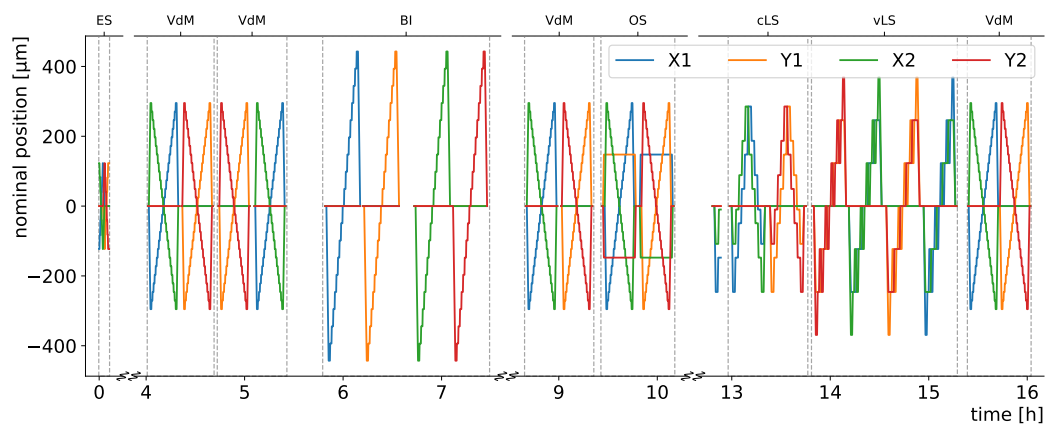
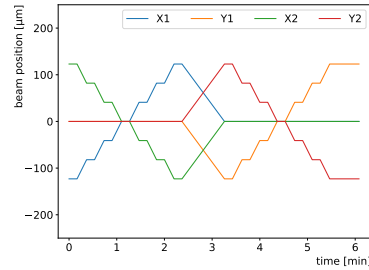


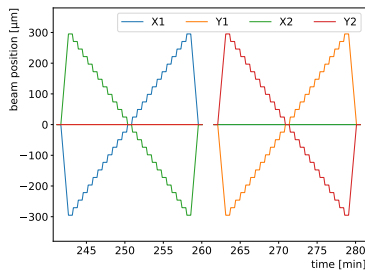
Fig. 4.2.: The nominal beam position during VdM fill in 2017, or fill 6016. The transverse horizontal (X) and transverse vertical (Y) are shown for beam 1 and 2 separately. Note the breaks in the time axis.

4.4.1 Emittance scans

The first scan appearing in figure 4.2 is an *emittance scan* (ES). This type of scan is not typical to the VdM fill but also appears in many physics fills. Essentially, an ES is a very short VdM scan with shorter measurements at fewer positions. From this, one can make a rough measurement of σ_{vis} without losing too much time for physics data taking. The ES estimates of σ_{vis} are useful to monitor the stability and linearity of the luminometers.



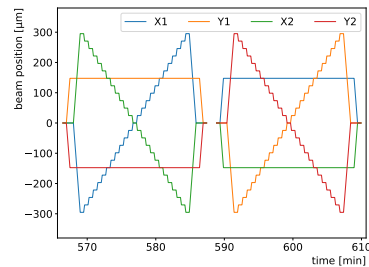
4.4.2 Van Der Meer scans



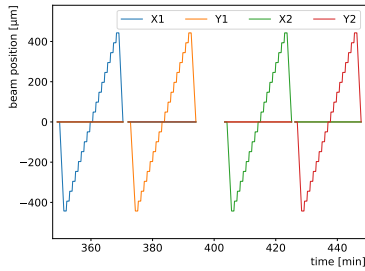
Next in line is the VdM scan, which is a more elaborate version of an ES. They consist of two subscans of 25 steps each 30 sec long. Between consecutive steps, the beams are moved about $25\ \mu\text{m}$ in opposite directions so that the maximum separation reaches about $600\ \mu\text{m}$. During the VdM scans, the actual measurement of σ_{vis} takes place. The symmetric beam movement has the advantage that it can achieve a large separation, which benefits the precision of the VdM fits described earlier.

4.4.3 Off-set scan

Off-set (OS) scans are similar to VdM scans but have an additional offset in the plane perpendicular to the scanning plane. In this way, one can probe a part of the transverse plane different to the X - and Y -axis, making it possible to evaluate the factorization bias. However, the large separation in OS scans also means much lower statistics, which might be background dominated for some luminometers. In that case, OS scans can still serve as a background measurement that can be subtracted from the VdM scans.



4.4.4 Beam Imaging scan



In beam imaging (BI) scans, one of the beams remains stationary while the other is moved over it. The goal is to use the moving beam as a scanner to make a profile image of the other beam. That works as follows. When the moving beam moves by a vector $\vec{\delta}$, the event count dN over a time Δt in a small area dA around \vec{x} will be $dN \propto f_1(\vec{x})f_2(\vec{x} + \vec{\delta})dA$. Integrating over $\vec{\delta}$ eliminates the the density f_2 as it

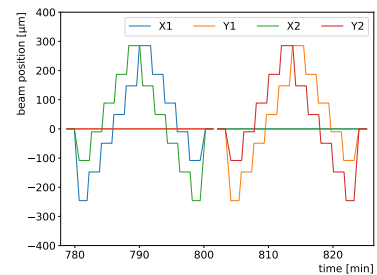
is normalised to unity: $\int (dN/dA)d\vec{\delta} \propto f_1$. Therefore, the event density integrated over the scan tells us the beam profile of the stationary beam.

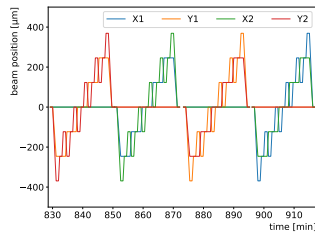
BI scans require a detector that can localise the events in the transverse plane. At CMS, such a detector is the silicon tracker: a cylindrical silicon detector installed directly around the collision point. It measures the tracks of the particles created in the collisions and traces those tracks back to points where a collision took place. Such points are called vertices.

The BI scans can serve as a method for evaluating the factorization bias and correcting it. One can even use them as an independent measurement of A_{lum} , which only depends on the profile functions. However, the vertex reconstruction precision also limits the use of BI scans.

4.4.5 Length scale scans

The goal of length scales (LS) scans is to determine for both beams the length scale factors α_x and α_y introduced in section 4.3.1. In a constant LS scan, this is done by putting the beams at constant separation d and moving them in parallel. One then uses the data from the CMS tracker, introduced in section 4.4.4, to determine the so-called beam spot, which is the point of highest collision rate. To a good approximation, this is simply the average of both beam positions. If the beams move with scale factors α_1 and α_2 , then the beam spot will move with a scale factor $(\alpha_1 + \alpha_2)/2$. If $\alpha_1 = \alpha_2$, then d will remain constant and so will the event rate. Conversely, from the change in event rate, one can infer $\alpha_1 - \alpha_2$.





An alternative method that the CMS collaboration only recently implemented is the variable LS scan [16, 17]. In such a scan, one “non-scanning” beam is moved to different positions, while the other “scanning” beam performs a three-step mini scan around each of those positions. From the mini scans, one can estimate the position of the beam spot when the beams would collide head-on, which coincides with the position of the non-scanning beam. Hence, one can directly extract the length scale factor for the non-scanning beam.

4.5 The CMS luminosity measurement from 2015-2016

The last publication on luminosity of the CMS collaboration reported the results for 2015 and 2016 [15]. The analysis of those two years achieved an uncertainty of 1.6 % and 1.2 % respectively. The analysis of 2017 and 2018 is still ongoing, although preliminary results are already available [16, 17].

The contributions to the overall uncertainty in 2015 and 2016 are shown in table 4.1. There is no clearly effect, but rather a lot of smaller uncertainties ranging from 0.1 % to 0.5 %. However, the uncertainties related to the beam positions contribute substantially, through the length scale, (coherent) beam-beam effects, orbit drift, and the residual differences. The study of the beam positions is, therefore, important to achieve an even more precise luminosity measurement.

Source	2015 [%]	2016 [%]	Corr
Normalization uncertainty			
<i>Bunch population</i>			
Ghost and satellite charge	0.1	0.1	Yes
Beam current normalization	0.2	0.2	Yes
<i>Beam position monitoring</i>			
Orbit drift	0.2	0.1	No
Residual differences	0.8	0.5	Yes
<i>Beam overlap description</i>			
Beam-beam effects	0.5	0.5	Yes
Length scale calibration	0.2	0.3	Yes
Transverse factorizability	0.5	0.5	Yes
<i>Result consistency</i>			
Other variations in σ_{vis}	0.6	0.3	No
Integration uncertainty			
<i>Out-of-time pileup corrections</i>			
Type 1 corrections	0.3	0.3	Yes
Type 2 corrections	0.1	0.3	Yes
<i>Detector performance</i>			
Cross-detector stability	0.6	0.5	No
Linearity	0.5	0.3	Yes
<i>Data acquisition</i>			
CMS deadtime	0.5	<0.1	No
Total normalization uncertainty	1.3	1.0	—
Total integration uncertainty	1.0	0.7	—
Total uncertainty	1.6	1.2	—

Tab. 4.1.: Contributions to the errors of the CMS luminosity measurement in 2015-2016. The upper half (normalization) refers to the σ_{vis} measurement, while the lower half (integration) shows all uncertainty that arises in using the luminometers over an extended time period. Table from [15].

Beam Position Monitor Studies

” *The distance between insanity and genius is measured only by success.*

— **Bruce Feirstein**

American screenwriter and humorist

The previous section introduced the problems arising as soon as one starts displacing the beams. The uncertainties introduced through those problems make substantial contributions to the total luminosity uncertainty. In this chapter, I will assess the phenomena affecting the beam positions by looking at the data provided by the beam position monitors (BPMs) during fills 6016 and 6868 in 2017 and 2018, respectively. The goal is to subtract the effects we already understand and look into what remains for new phenomena, like the hysteresis effect.

5.1 The data

The previous chapter showed the positions of the beams throughout the VdM fill. Those positions are nominal and only roughly represent the real beam positions. To get information about the true positions, the LHC provides two separate BPM systems: the arc BPMs and the DOROS BPMs. Figure 5.1 gives a data fragment from the fourth and fifth hours of the VdM fill in 2017. It shows two VdM scans, which contain subscans in the X and Y planes. The data consists of X and Y coordinate for both beams every second. I will refer to these four coordinates collectively as beam coordinates. The full data for both VdM fills in both years can be found in appendix A.

One can see that the arc and DOROS BPMs show very different pictures of the same event. The reason is that both systems perform measurements at different places in the ring. The DOROS BPMs are located right next to the collision point, at 21.6 m on both sides. That is well within the range of the corrector magnets that move the

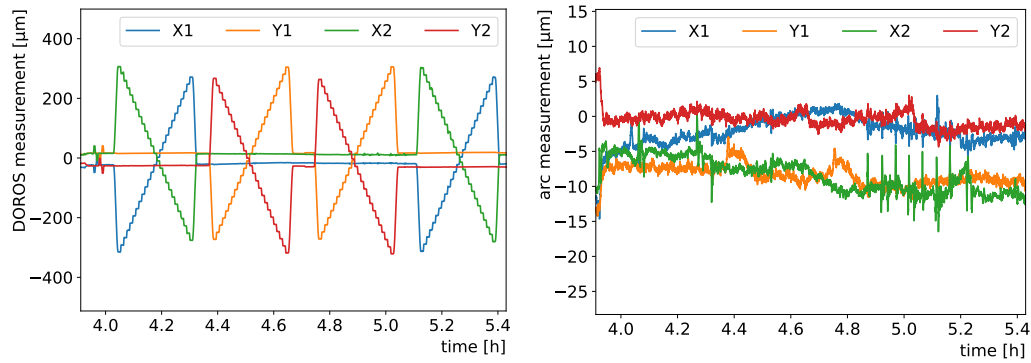


Fig. 5.1.: DOROS (left) and arc (right) BPM measurements during the two first VdM scans from fill 6016 in 2017.

beams during the VdM fill. That is why the full nominal movement appears in the DOROS BPMs.

The arc BPM measurement works differently. It uses a set of arc BPMs in the interaction point (IP) neighbourhood, but those are still outside the corrector magnets. An LHC optics model takes in all these measurements and predicts the position at the IP itself. However, this model does not take into account the corrector magnets. For that reason, there is no movement visible in the arc data.

Note that the beam coordinates appear shifted relative to each other in both the arc and DOROS BPMs. This offset is a measurement artefact that does not represent a physical shift. I subtracted these offsets using optimisation scans: the wiggles visible in figure 5.1 in the DOROS data on the extreme left. The LHC uses these small wiggles to align the beams in a perfectly head-on configuration. After the optimisation scans, the beams should be at $x = y = 0$, so any remaining shift in the BPM data may be considered an unphysical offset.

5.2 Effects

The goal is to model the BPM data as a function of the nominal position taking into account all the effects discussed in section 4.3. Figure 5.2 illustrates how each effect manifests itself in the data.

We see that the DOROS data with the nominal positions subtracted still correlate with the nominal positions, both in the plane of the nominal movement and in the perpendicular plane. That could be due to length scale and misalignment effects. It is important to note here, that these effects not only reflect the response of the

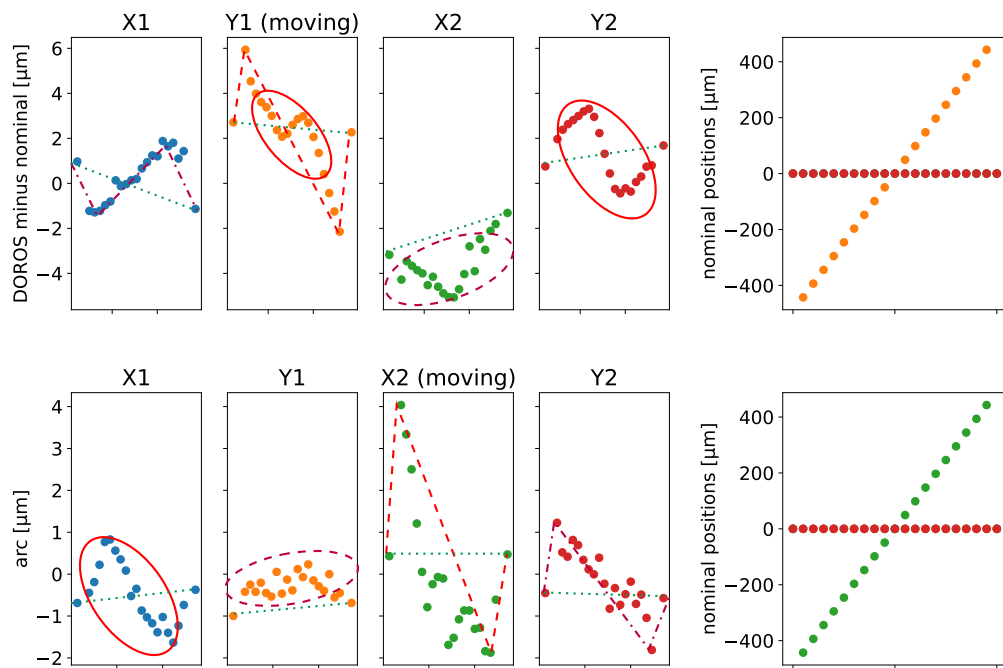


Fig. 5.2.: Illustration of the different effects affecting the position: length scale factor (red dashed), misalignment (purple dashed-dotted), linear orbit drift (green dotted), beam-beam deflection (red ellipse), and unexplained movement (purple dashed ellipse). The plots are only for illustrative purposes and have been selected because they show pronounced effects. The upper figures show the DOROS measurements with the nominal positions subtracted during a BI scan in the Y plane from fill 6868 in 2018. The lower figures show the arc measurements from a BI scan in the X plane from fill 6016 in 2017. Note that length scale and misalignment in the case of the arc refer to leakage.

corrector magnets, as explained in section 4.3.1. If the DOROS BPMs measure at a different scale or are slightly tilted, the same effects will occur as those seen in figure 5.2.

In figure 5.2, one can see that the arc data also show effects reminiscent of length scale and misalignment, even though the arc BPM should be insensitive to the movement during the VdM fill. This phenomenon, called leakage, is caused by the imperfect balancing of the corrector magnets, because of which the beams are not moved back to their original orbit when leaving the interaction area. I will also refer to these leakage effects as length scale and misalignment, although one should keep in mind that this length scale does not refer to the length scale of the actual beam motion. Moreover, imperfections of the arc BPMs will also influence the arc length scale and misalignment.

The second effect that catches the eye is the beam-beam deflection. It shows as a sinusoidal shape in the moving plane in both DOROS and arc measurements, although only clearly in one beam for the latter. The shape roughly matches the prediction of formula equation (4.5) as shown in figure 4.1. However, the observed deflection does not directly reflect the true deflection at the IP. Not all bunches in the VdM fill collide, so the observed deflection is a potentially complicated average of deflected and undeflected bunches. Furthermore, the DOROS BPMs measure at 21.6 m. As the beam-beam deflection also makes the bunches move at a slight angle, DOROS will see a more pronounced displacement than predicted by equation (4.5). Finally, some unexplained effects remain, including random orbit drift and unknown systematics. For instance, the positions before and after each scan in figure 5.2 have changed. Sometimes, beam coordinates move, although they should not, in principle. That happens, for instance, X_2 above and Y_1 below in figure 5.2.

5.3 Orbit drift

I will now estimate the effects listed above from the data and subtract them for every scan separately. The word “scan” in this context refers to a regular series of steps between two longer periods in which the beam is nominally head-on. For example, the VdM procedure takes two scans, one in the X -plane and one in the Y -plane. The two rows in figure 5.2 also represent two scans.

In this section, I will discuss orbit drift. The estimation used linear interpolation between two self-defined 30 s intervals right after and before each scan. Figure 5.3 shows an example of this procedure. This type of estimate models the orbit drift as

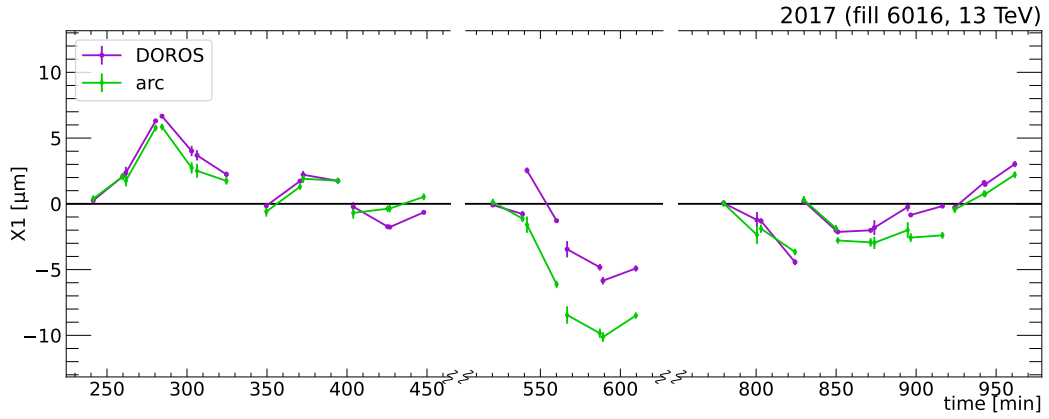


Fig. 5.3.: Linear orbit drift obtained from linear interpolation between the nominally head-on positions before and after each scan. The scans do not include emittance scans. The dots represents the mean position along the X -axis of beam 1 during the step, while the bars show the spread of the BPM measurements within the step.

a linear effect and is, therefore, referred to as a *linear orbit drift* correction. If the orbit drift proceeds slowly, such a model should work well.

Two different BPM systems are available to determine the orbit drift, which allows for a cross-check of the results. From figure 5.3, it looks like both systems agree reasonably well, although, for some scans, there is a significant offset between them. That is more clearly visible in figure 5.4. This figure compares the two systems in the interpolated drift in the scan centre c_{LD} on the left and the slope δ_{LD} on the right. Overall, the arc and DOROS BPMs measure similar values for these parameters. Individual scans can, however, disagree. Especially c_{LD} seems to differ between the two BPMs. That suggests that the offset subtraction (see section 5.1) does not work perfectly. Figure 5.5 also supports this observation. It shows the difference between the DOROS and arc BPMs as a function of the time since the last optimisation scan. The more time elapses, the more the DOROS and arc BPMs tend to diverge. This issue seems more outspoken in fill 6016 than in fill 6868.

5.4 Length scale

Once I had subtracted the linear orbit drift from the data, I removed all other effects from the data simultaneously. More precisely, given a coordinate u of a beam (e.g. $X1$), with perpendicular coordinate v (e.g. $Y1$), I fitted the following model:

$$u_{\text{BPM}}(t) = \alpha u_{\text{nom}}(t) + \beta v_{\text{nom}}(t) + \gamma \Delta u_{\text{BB}}(t). \quad (5.1)$$

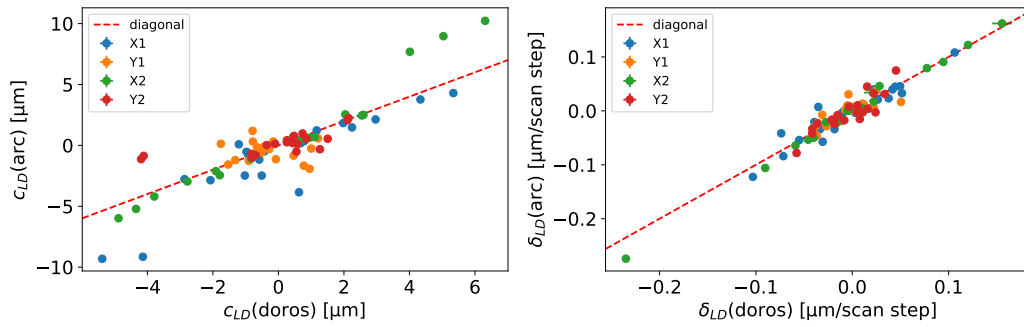


Fig. 5.4.: Comparison between the arc and DOROS measurements during fill 6016 of the interpolated orbit drift slope δ_{LD} and the linear orbit drift interpolated to the scan centre c_{LD} . Every points represents the orbit drift during one scan along one axis for one beam, (e.g. $X1$ during the first VdM scan in the Y plane).

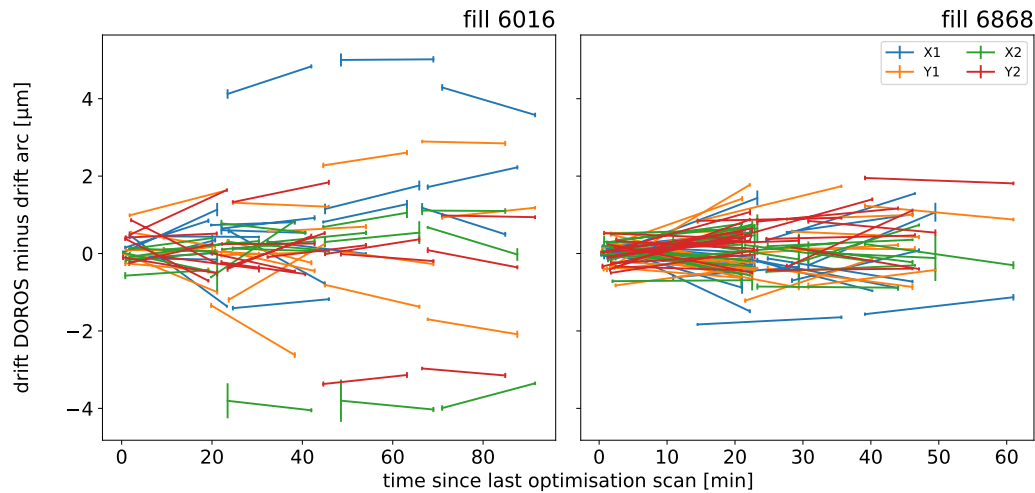


Fig. 5.5.: Difference Δ between the arc and DOROS measurements of the positions at the head-on steps before and after each scan as a function of the time elapsed since the last optimisation scan. The lines represent the orbit drift interpolation during the scan. Error bars represent the errors on Δ derived from the spread on the BPM measurements within each step.

Here, α represents the length scale effect, β the misalignment, and Δu_{BB} the beam-beam deflection. This fit has been performed for every BPM and beam coordinate independently. Note that for most cases, this fit has only two free parameters at most since only during OS scans u_{nom} and v_{nom} can be simultaneously non-zero. In some fits, β is the only free parameter. For instance, this is the case in a fit to the $Y1$ coordinate in a VdM scan in the X plane.

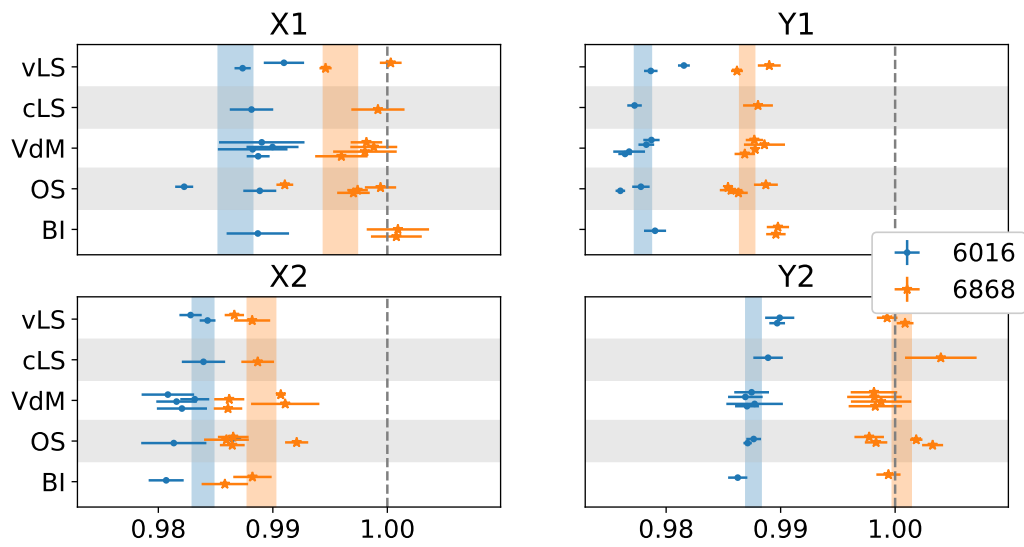
Figure 5.6(a) shows the values of α for the DOROS data from fills 6016 and 6868. Note that all values are close to unity, which expresses that the DOROS BPMs are within the corrector magnets so that $u_{\text{DOROS}} \approx u_{\text{nom}}$ to the lowest order. It is, however, clear that the scale measured by the DOROS BPMs deviates consistently from the nominal scale. Another observation is that the values of α are consistently higher in fill 6868 than in fill 6016. This is not unexpected since both fills are in different years, and the response of the corrector magnets could have changed in the meantime. Note, however, that it could also have been the response of the DOROS BPMs themselves that explains these observations.

In general, the values obtained from different scans are reasonably close to each other. Nevertheless, individual fits are often inconsistent with each other based on the fit uncertainties. That suggests that the value of α can fluctuate from scan to scan. I computed a weighted average $\bar{\alpha} = (\sum_i \sigma_i^{-2})^{-1} \sum_i \alpha_i \sigma_i^{-2}$ for every beam coordinate, whose uncertainty I evaluated as

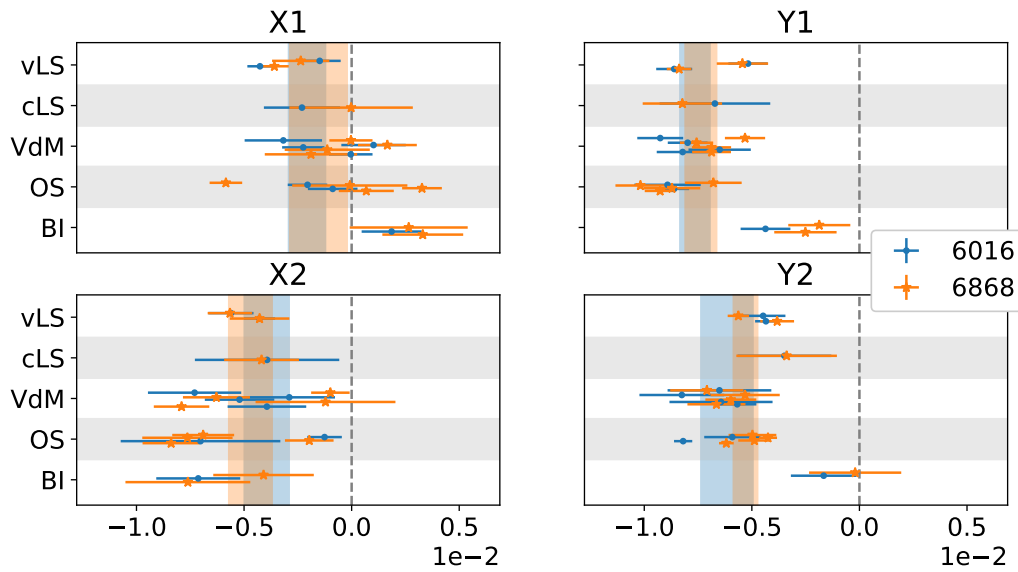
$$\text{Var } \bar{\alpha} = \left(\sum_i \sigma_i^{-2} \right)^{-2} \sum_i \sigma_i^{-4} \text{Var } \alpha_i = \left(\sum_i \sigma_i^{-2} \right)^{-1} + \left(\sum_i \sigma_i^{-2} \right)^{-2} \sum_i \sigma_i^{-4} \hat{\sigma}^2. \quad (5.2)$$

$\hat{\sigma}^2$ represents the scan to scan variance of α , which I evaluated by calculating the spread of all α_i weighted by their fit uncertainty.

We can also look at the value of α when fitting equation (5.1) to arc data. Recall that the arcs should to the lowest order not see any movement that correlates with the nominal movement, as their location is outside the corrector magnets. In other words, $\alpha \approx 0$, as one observes in figure 5.6(b). However, figure 5.6(b) also shows a consistent deviation from zero in all beam coordinates, but $X1$. There is, therefore, strong evidence that the movement in the region within the corrector magnets leaks outside. Furthermore, the value of α does not significantly change between the two fills, contrary to the DOROS measurements.



(a) Length scale factors derived from fits to DOROS data.



(b) Length scale factors derived from fits to arc data.

Fig. 5.6.: Length scale factors for fill 6016 and fill 6868. The vertical bands represent a 1σ confidence interval for average of all scans weighted the fit uncertainties. Note that every displayed point for a given beam coordinate (say $X1$) corresponds to a scan in which there was nominal movement along that coordinate.

5.5 Misalignment

The second parameter in equation (5.1), β , expresses the misalignment of either the corrector magnets or the BPMs. Its value should be zero to the lowest order, and one can see in figure 5.7 that this is the case. Many scans show values of β that differ significantly from zero, but there is only an outspoken overall deviation from zero in the DOROS data of beam one. In this case, the average β is positive for both coordinates, suggesting a more complicated effect than just a rotated coordinate frame. In the case of a simple rotation, one would expect opposite signs.

5.6 Beam-beam deflection

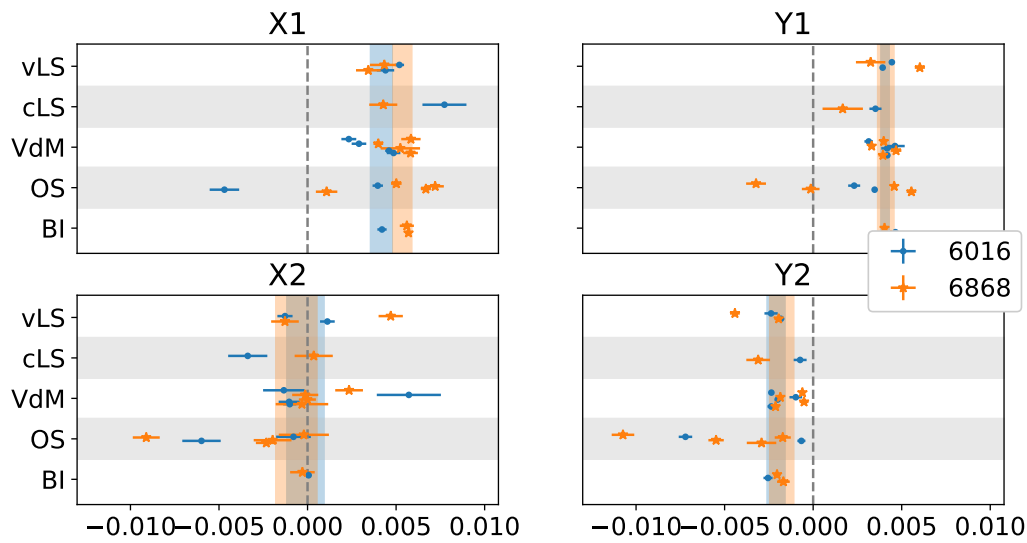
Finally, we will discuss the γ parameter in equation (5.1). There are two reasons why γ would differ from one, i.e., why the observed deflection differs from the prediction of equation (4.5). First, not all bunches collide, which means some bunches deflect while others remain unperturbed. It is not straightforward to predict the effect on the deflection measured by the BPMs, but a reasonable guess is that the observed deflection will be lower by a factor γ_D called the dilution factor. A reasonable value for γ_D would be the fraction of the bunches that collide, which is 0.62 in fill 6016 and 0.89 in fill 6868.

Second, the beam-beam deflection makes the beams move at an angle $\theta/2$ away from each other with θ given by equation (4.3). When travelling a distance s after the collision, one can see from simple trigonometry that displacement will grow according to

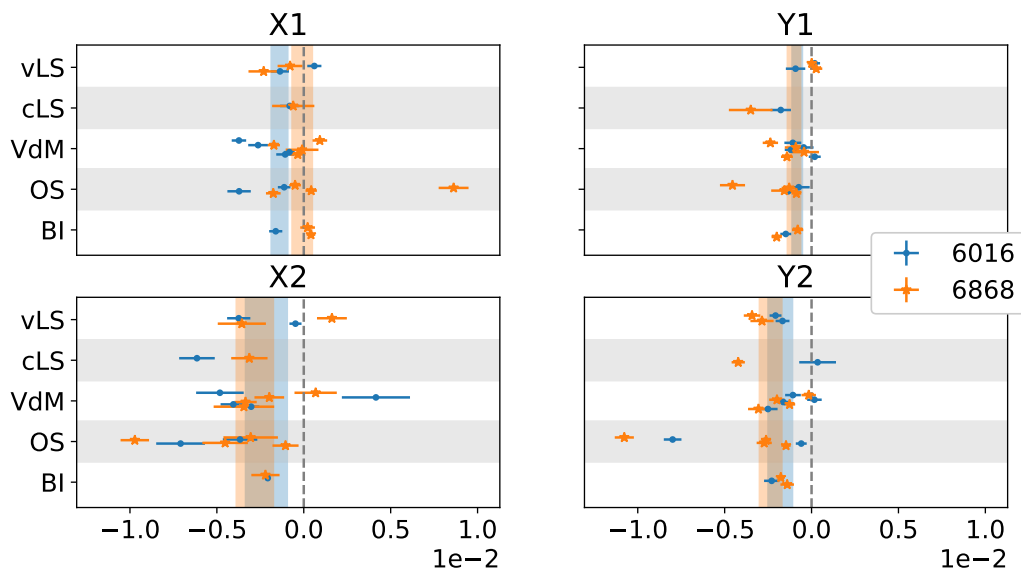
$$\Delta u_{\text{BB}}(s) = \Delta u_{\text{BB}}(0) + s\theta/2 = (\beta^* \cot \pi Q + s)\theta/2 = \left(1 + \frac{s}{\beta^* \cot \pi Q}\right) \Delta u_{\text{BB}}(0),$$

where we used equation (4.4). Note that this formula becomes invalid on entering the LHC magnet systems.

The effect of the angle should not affect the arc BPMs since those measurements are extrapolations to the collision point itself. But the DOROS BPMs measure at a distance of 21.6 m. That means DOROS measures a deflection that is a factor 2.65 larger in the X direction and a factor 2.78 in the Y direction using the beams optics parameters at IP5. The usual name for this factor is the geometrical factor γ_G . It carries some uncertainty on its value mainly because of the uncertainty on β^* , which is about 15% at IP5 for fills 6016 and 6868 [72].

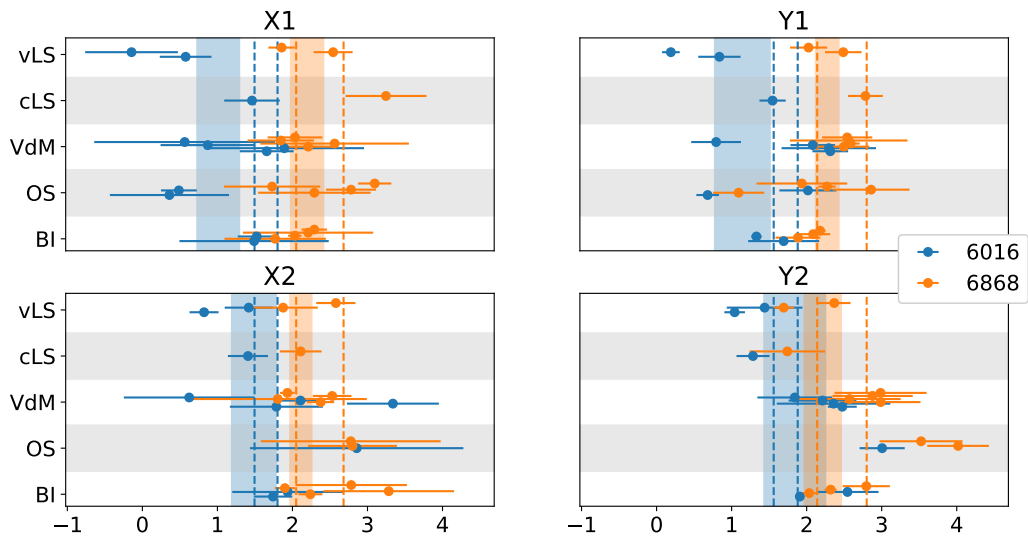


(a) Misalignment factors derived from fits to DOROS data.

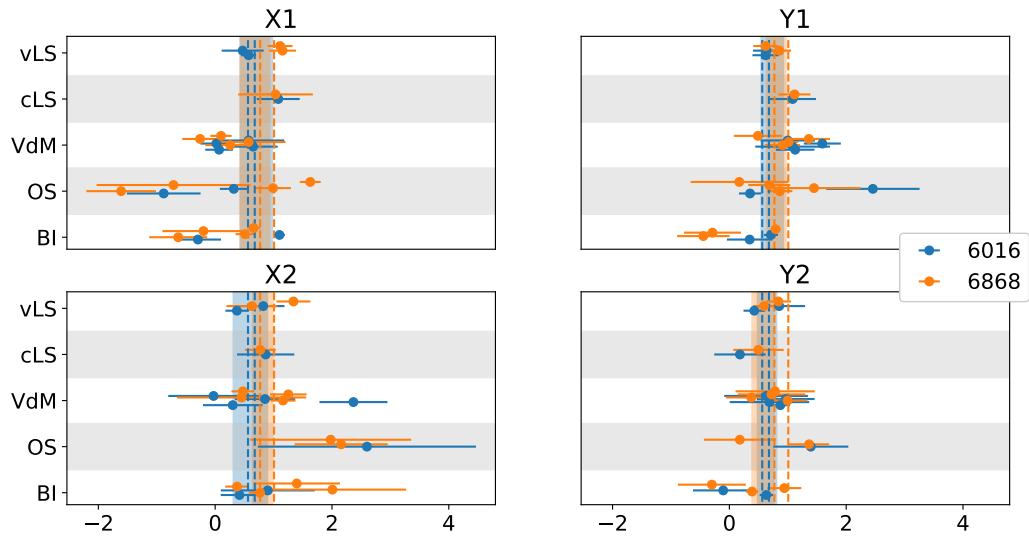


(b) Misalignment factors derived from fits to arc data.

Fig. 5.7.: Misalignment factors for fill 6016 and fill 6868. The vertical bands represent a 1σ confidence interval for average of all scans weighted the fit uncertainties. Note that every displayed point for a given beam coordinate (say $X1$) corresponds to a scan in which there was nominal movement along the beam coordinate perpendicular to it (i.e. $Y1$).



(a) Modifying factors of the beam-beam deflection from fits to DOROS data



(b) Modifying factors of the beam-beam deflection from fits to arc data.

Fig. 5.8.: Modifying factors of the beam-beam deflection for fill 6016 and fill 6868. The vertical bands represent a 1σ confidence interval for the average of all scans weighted by the fit uncertainties. The dashed lines show the 1σ interval for the expected value $\gamma_D \gamma_G$. Note that every displayed point for a given beam coordinate (say $X1$) corresponds to a scan in which there was nominal movement and thus deflection along that coordinate.

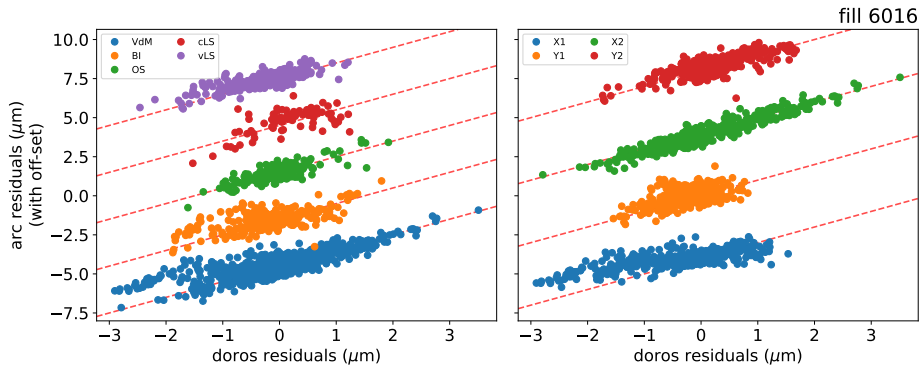


Fig. 5.9.: Residuals from the arc data versus those of the DOROS data. The left plot shows the residuals grouped by scan type, the right plot grouped by beam coordinate. Each group has been given an offset along the vertical axis. The diagonal dashed line is shown for reference.

Figure 5.8 shows the results for γ . The overall image is rather chaotic, but the (weighted) averages seem consistent with the value $\gamma_D\gamma_G$ from the discussion above.

5.7 Residuals

We have now considered all understood effects and subtracted them from the data. We are now interested in the residuals. These will include random non-linear orbit drift, unaccounted systematic effects, and BPM related noise. However, one should be mindful that some of these latter effects might have mimicked the understood effects. In that case, the fits will have subtracted them as well.

As we have two BPM systems, we can compare them to get an idea of how much of the residuals represents BPM related noise rather than physical displacements of the beam. Figure 5.9 shows such a comparison for fill 6016. The residuals are grouped according to their type on the left and their beam coordinate on the right. The figure reveals a strong correlation between the residuals from both BPM systems: they strongly align with the diagonal dashed line, which corresponds to equal residuals. This happens for all scan types and all beam coordinates, although some systematic deviation can be observed in the X -coordinate of beam 1. Figure 5.10 shows the 3σ covariance ellipse for the ungrouped residuals in both fill 6016 and fill 6868. The deviations away from the diagonal are up to a few exceptions at most $1.0\mu\text{m}$ large, which suggests that a significant part of the residuals represents a real effect in the beam positions and not just detector noise.

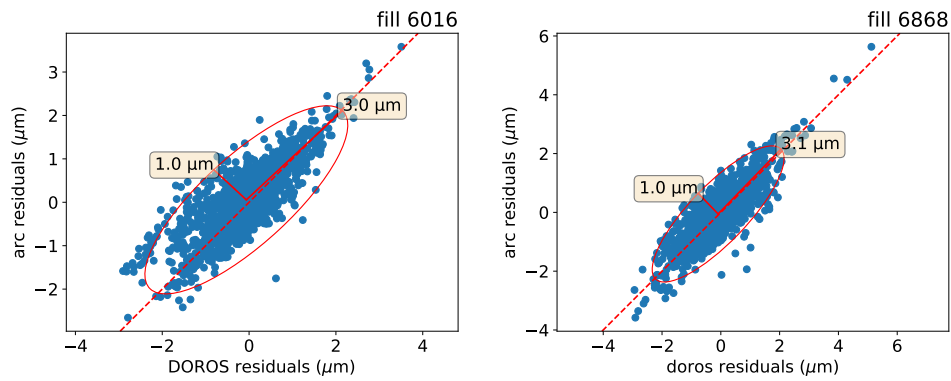


Fig. 5.10.: Residuals from the arc data versus those of the DOROS data and their 3σ covariance ellipse. The left shows residuals from fill 6016, the right from fill 6868. The length of the ellipse half axes are displayed.

The question now is whether this real effect is systematic, random, or both. We can get an idea from this by looking at the residuals themselves as a function of time. One should only look at the beam coordinates for which there was also nominal movement since the residuals are most likely only random in the other beam coordinates. For instance, in a VdM scan in the X plane, only the residuals for the $X1$ and $X2$ coordinates are of interest. Note that one cannot compare different types of scans directly since the differences in movement may alter systematic effects.

Figure 5.11 shows the residuals for the VdM scans in fill 6016 with the average over the available scans for every beam coordinate and step. The result reveals some systematic symmetric shape of about a micrometre in size. Beam one shows systematic deviation towards negative residuals, while beam two exhibits the opposite. However, there is also scan-to-scan variation besides this systematic movement which is often similar in size. That suggests a significant random non-linear orbit drift knowing that the DOROS and arc residuals tend to agree rather well on the residuals.

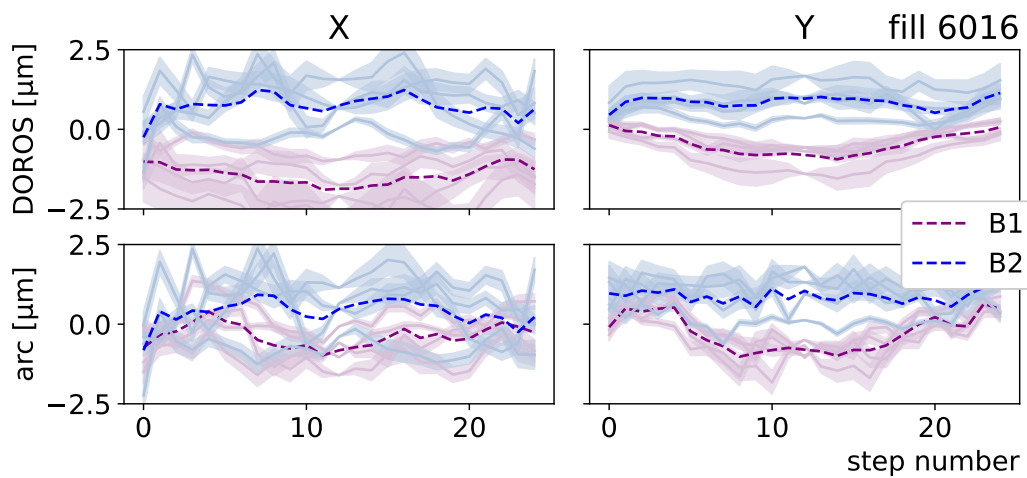


Fig. 5.11.: Residuals of arc and DOROS data from the VdM scans in fill 6016. Only the beam coordinates for which there is also nominal movement are considered. The colored bands are errors derived from the fit. The dashed line shows the average residuals over the different scans. The horizontal axis shows the step number.

A rudimentary Van Der Meer analysis

” *Science discovery is an irrational act. It’s an intuition which turns out to be reality at the end of it. I see no difference between a scientist developing a marvellous discovery and an artist making a painting.*

— **Carlo Rubbia**

Italian particle physicist at CERN

To conclude the analysis, I performed a VdM analysis and applied corrections to the positions based on the discussion in chapter 5. The goal is to assess how such corrections affect the luminous area and what uncertainty they introduce. I only considered corrections to the moving beam coordinates, leaving the stationary beam coordinates for future work. So this analysis does not cover misalignment and drift of the non-moving beam coordinates. It neither discusses length scale because there are separate ongoing efforts dedicated to this issue.

6.1 Vertex counts

As luminometer, I used the number of vertices counted by the CMS silicon tracker (see sections 4.4.4 and 4.4.5) averaged per bunch crossing. Because of the specifics of a VdM fill, this vertex number per bunch-crossing is on the low side. In fill 6016, it was around 0.2 during head-on collisions. CMS did not record vertices for all pairs of colliding bunches but only for five selected ones in each fill. These pairs are identified by their bcid number, which indicates the slot number in which the colliding bunches are located. (See section 2.2.) In fill 6016, CMS performed measurements bcids 41, 281, 872, 1783, and 2063. In fill 6868, the bcids are 265, 865, 1780, 2192, and 3380.

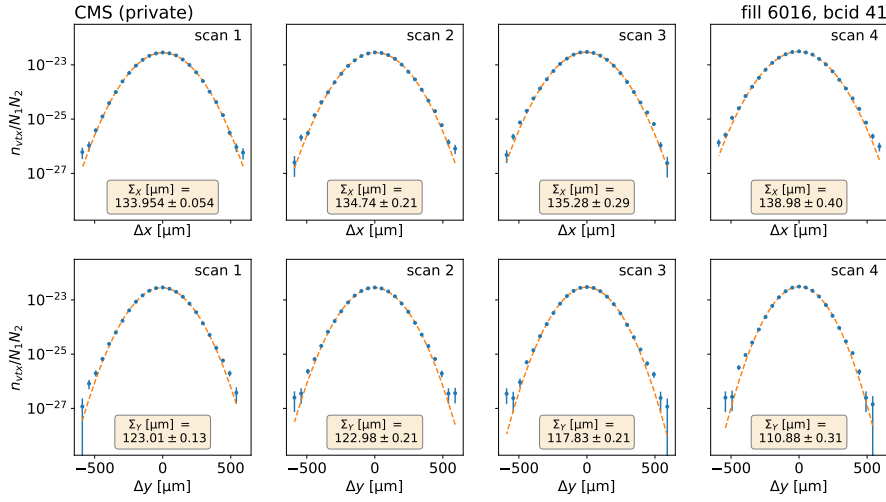


Fig. 6.1.: VdM scans for fill 6016 with vertex counts recorded in one pair of colliding bunches (BCID 41) by the CMS silicon tracker. The displayed VdM scans use uncorrected nominal positions. The upper row are the VdM scans along the X -axis, the lower row along the Y -axis. The points are the measured average number of vertices per crossing normalised to the product of the proton numbers in each bunch. The dashed line is a Gaussian function fitted to this data. The values for the width $\Sigma_{X,Y}$ of this Gaussian are shown for each scan.

6.2 Without corrections

I will first illustrate the VdM fit procedure using the uncorrected nominal data. The model I used is a simple Gaussian model,

$$\ln n_{\text{vtx}}(u) = \ln N_0 - \frac{1}{2\Sigma^2}(u - u_0)^2, \quad (6.1)$$

with $u = \Delta x, \Delta y$ and n_{vtx} the average number of vertices per bunch crossing. This model is linear with parameters $a = \ln N_0 - u_0^2/2\Sigma^2$, $b = u_0/2\Sigma^2$, and $c = 1/2\Sigma^2$, so ordinary least squares methods suffice to fit it. However, the error on n_{vtx} grows as the displacement increases because of a drop in statistics. It makes, therefore, sense to use a weighted least squares method instead. Using simple error propagation, we can find $A = 2\pi\Sigma_X\Sigma_Y$ (see section 4.2) from the values of c determined in the two scans of a VdM scan pair. From the luminous area, we can determine σ_{vis} using equations (3.1) and (3.3) applied at the peak rate N_0 derived from the fit:

$$\sigma_{\text{vis}} = \frac{N_0 A_{\text{lum}}}{\nu N_1 N_2}. \quad (6.2)$$

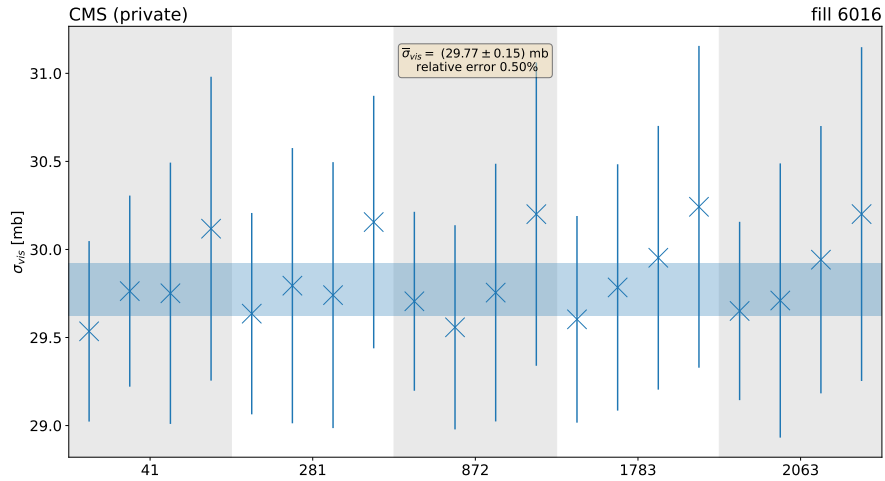


Fig. 6.2.: Calculated values of σ_{vis} based on average number of vertices per crossing for all recorded bcids in fill 6016. For every bcid, there are four values corresponding to the four VdM scans performed during this fill. A 1σ confidence interval is shown for the weighted average.

Before we can apply this formula, a few changes are needed. First, because we are looking at the vertices *per crossing*, we can leave the frequency out of equation (6.2). Second, it is better to renormalise the average number of vertices per bunch crossing to the product of the proton numbers in each bunch, i.e., use n_{vtx}/N_1N_2 . This accounts for the slight decrease in protons in the bunches due to the collision during the crossings. If one does so, then N_1N_2 also disappears in equation (6.2). Finally, because every bunch pair can have different values for A_{lum} , N_1 , and N_2 , I performed the VdM scans for every bcid separately.

Figure 6.2 presents the results of the fits using the renormalised average vertex numbers for bcid 41 in fill 6016. The Gaussian fits the data mostly well, although it slightly underestimates n_{vtx} at large displacements. That means that the calculated A_{lum} may be somewhat too low, although the effect cannot be large. Figure 6.1 shows the results for σ_{vis} for all bcids in all four VdM scan pairs. All values are compatible with each other. The average value $\bar{\sigma}_{\text{vis}}$ is 29.77(15) mb, assuming that all these estimates are uncorrelated. That is reasonable for different scan pairs, but less so for different bcid within the same scan pair. This is also suggested by figure 6.1 where a similar pattern repeats itself for every bcid. The error on $\bar{\sigma}_{\text{vis}}$ may, therefore, be too low. However, the following will mostly focus on how the estimates of σ_{vis} change because of to the positions. The absolute sizes matter less.

6.3 Linear orbit drift

In the next step, we can evaluate the effect of correcting for linear orbit drift (LD). We have two BPM systems that can provide this correction: the DOROS and the arc BPMs. Comparing the two inputs provides a size estimate of the uncertainty associated with this correction.

Figure 6.3 shows the results of the LD correction using the average of the DOROS and arc systems. As seen in the middle panel, there is no large effect on the fit errors. That is a consequence of the linearity of the correction, which for the most part only rescales u and, therefore, the width Σ . The spread of the four scan pairs decreases suggesting the correction brings us closer to the truth (right panel). The values of σ_{vis} change by at most 0.4 % (left panel) and most of this change disappears when taking the weighted average. Furthermore, the difference between using arc or DOROS data, which is shown as an error bar in figure 6.3, is only about 0.05 %. Therefore, the uncertainty of this correction can be assumed to be small.

6.4 Beam-beam deflection

The second correction is the beam-beam deflection (BB), shown in figure 6.3 together with the LD correction. The main uncertainty on this correction is from the uncertainty on β^* . For all scan pairs, the effect is a 1 % increase of σ_{vis} if compared to the value with only an LD correction. The fit errors drop significantly by up to 10 %, suggesting again that this correction improves the situation. The spread remains almost the same. That might be because the correction is nearly the same for all scan pairs and bcids.

6.5 Residuals

Finally, we can use the residuals from the fits to the BPM measurements as an additional correction on the positions. That assumes that the length scale and the beam-beam deflection are the only effects whose size depends on whether we measure with the DOROS or the arc BPMs. Doing this affects the VdM scans, as shown in figure 6.4. The values of σ_{vis} decrease for some scan pairs and increase for others, in different amounts for DOROS and arc residuals but not more than 0.1 %. The picture for the error on σ_{vis} is equally mixed, with changes up to 5 %.

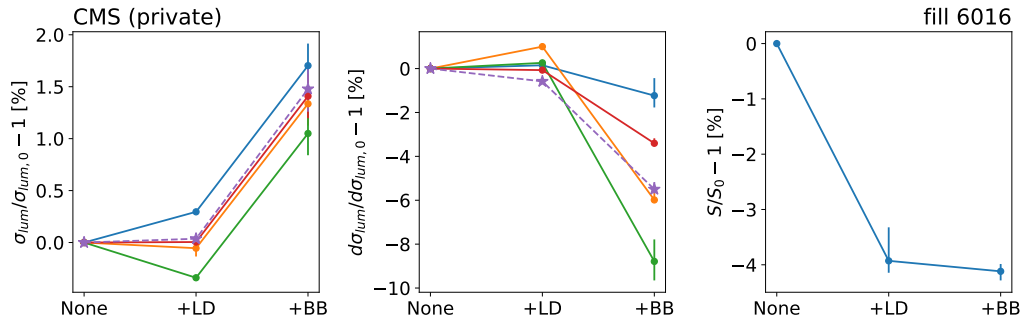


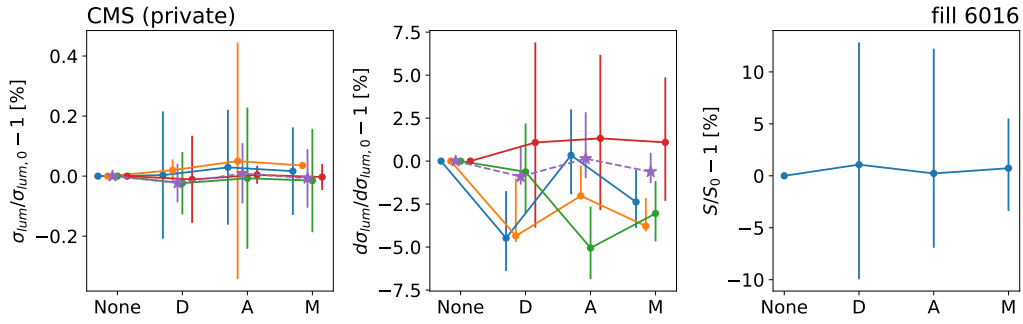
Fig. 6.3.: Effect on the values of σ_{vis} from fill 6016 when the positions are corrected for linear orbit drift (+LD), and for beam-beam deflection (+BB). The left shows σ_{vis} itself, the middle the error $d\sigma_{\text{vis}}$, and the right the spread S of σ_{vis} over the four scan pairs. All three quantities are expressed a percentage change relative to their value if no corrections (None) are applied. The full lines on the left two plots show the four σ_{vis} estimates derived from bcid 41. The dashed starred lines shows the average $\bar{\sigma}_{\text{vis}}$ over all scan pairs and bcids, with the error on $\bar{\sigma}_{\text{vis}}$ computed as in equation (5.2).

The spread does up down slightly by about 1 %. From this, I cannot conclude that that this correction actually does any good. It is, however, clear that the effect on σ_{vis} is nearly negligible.

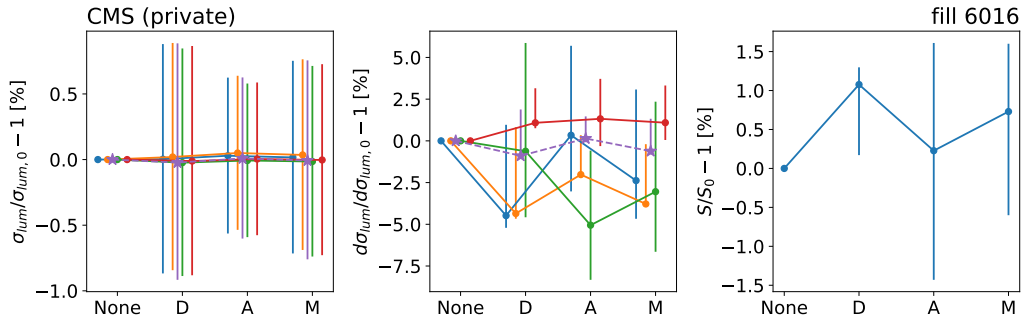
One should account for the uncertainty on the residuals as well. Firstly, one can calculate an uncertainty on the residuals from the uncertainty on the fit parameters in equation (5.1). Secondly, some drift effects might mimic the beam-beam deflection, which the fit of equation (5.1) to the BPM data subsequently subtracts. That might explain the variation in the fitted values of γ . One can argue that the same can happen with the length scale fits. However, this is a linear effect, so the linear orbit drift correction has already removed drift mimicking the length scale effect before fitting the model.

One can derive the fit covariance matrix on the residual vector $\vec{\epsilon}$ (i.e. the vector with the residuals as entries) from the covariance matrix of the parameters γ and α . From this ellipse, one can derive a 1σ covariance ellipse in the space of possible residual vectors, which is centred $\vec{\epsilon}$. It is two dimensional since the fit contains two parameters. I then selected a subset of the residual vectors on this ellipse and recalculated figure 6.4 for this selection. The error bars in figure 6.4(a) show the envelope of these calculations.

Finally, the uncertainty has to be derived that accounts for the beam-beam deflection-like drift that the fit might have wrongly subtracted when fitting equation (5.1). I did this by taking the spread $\hat{\sigma}$ (weighted by the fit errors) of the parameter γ over all scans during the fill. (See figure 5.8.) I did this separately for every fill and



(a) Error bars from varying the residuals by one σ , given their covariance matrix from the fit.



(b) Error bars from varying the amount of subtracted beam-beam deflection.

Fig. 6.4.: Effect on the values of σ_{vis} due to subsequent correction for residuals from DOROS (+D), arc (+A), and their average residuals (+M). The left shows σ_{vis} itself, the middle the error $d\sigma_{\text{vis}}$, and the right the spread S of σ_{vis} over the four scan pairs. All three quantities are expressed a percentage change relative to their value if only a LD and BB correction is applied (None). The dashed starred lines shows the average $\bar{\sigma}_{\text{vis}}$ over all scan pairs and bcids, with the error $\bar{\sigma}_{\text{vis}}$ computed as in equation (5.2).

beam coordinate. I then varied the value of γ by an amount $\pm\hat{\sigma}$, which means I changed the residuals of beam coordinate u by an amount $\hat{\sigma}\Delta_{\text{BB}}u$. The error bars in figure 6.4(b) show the outcome of that calculation. The uncertainty on the change in A_{lum} is of the order of 0.75 %, making it dominate the errors from figure 6.4(a).

6.6 Fill 6868

The above discussed fill 6016 in detail. This last paragraph summarises the results for fill 6868 in the year 2018. Figure 6.5 shows the derived visual cross-sections, which are again all mutually consistent. The average value has significantly decreased, which might reflect that the tracker has degraded over the year since the VdM scans of fill 6016 in 2017. If it has become less efficient at reconstructing vertices, then a decrease in σ_{vis} is not unexpected.

The effect of the position corrections are similar as in fill 6016, as figure 6.6 shows. Here, I used the mean of the DOROS and arc residuals to apply the last correction and added in quadrature the two types of errors shown in figure 6.4. The only difference with fill 6016 is the spread of the σ_{vis} values, which now increases because of the linear orbit drift correction. In fill 6016, I suggested that the observed decrease of the spread justified this correction, but given that the opposite happens in fill 6868, this argument seems rather weak. However, one should note that the spread is already small as it is, as figure 6.6 shows. An increase of a few per cent might, therefore, not be that meaningful.

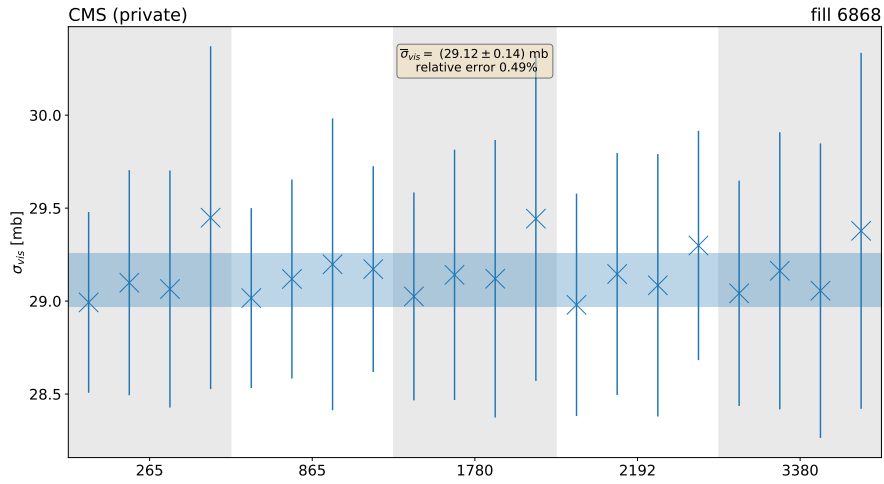


Fig. 6.5.: Calculated values of σ_{vis} based on average number of vertices per crossing for all recorded bcids in fill 6868. For every bcid, there are four values corresponding to the four VdM scans performed during this fill. A 1σ confidence interval is shown for the weighted average.

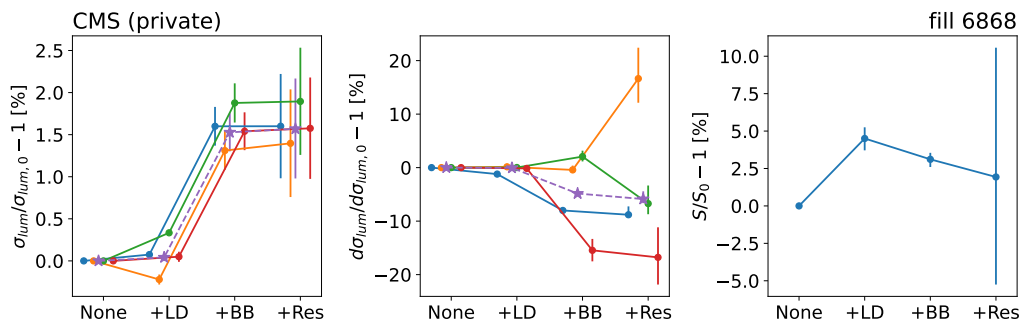


Fig. 6.6.: Effect on the values of σ_{vis} from fill 6868 when the positions are corrected for linear orbit drift (+LD), beam-beam deflection (+BB), and residuals (+Res). The left shows σ_{vis} itself, the middle the error $d\sigma_{\text{vis}}$, and the right the spread S of σ_{vis} over the four scan pairs. All three quantities are expressed a percentage change relative to their value if no corrections (None) are applied. The full lines on the left two plots show the four σ_{vis} estimates derived from bcid 265. The dashed starred lines shows the average $\bar{\sigma}_{\text{vis}}$ over all scan pairs and bcids, with the error on $\bar{\sigma}_{\text{vis}}$ computed as in equation (5.2).

Conclusion and outlook

“ *We changed again, and yet again, and it was now too late and too far to go back, and I went on. And the mists had all solemnly risen now, and the world lay spread before me.*

— **Charles Dickens**
English writer

Physicists have always strived for a universal theory describing the essence of our world. Luminosity is no part of that essence but no less essential. It is the key to unlocking the information enclosed in the cross-sections, which ultimately are of principal interest.

At the LHC, we use a clever method to determine its value with purely experimental input: the Van Der Meer method. This procedure infers one single cross-section from how our measurements change when the beams move around. With that cross-section, we can determine the luminosity at any given time.

The application of the Van Der Meer method comes, however, with a heap of ‘ifs’ and ‘buts’. One of the main problems arises in the core characteristic of the Van Der Meer procedure. How can we know precisely where the beams are? The nominal positions we enter in the machine differ from the realised positions for many reasons, some of which we do not understand. Beams deflect each other if they do not collide head-on. Scale differences occur, or reference frames may not align. Random changes in the LHC conditions can make the beams drift away.

In this thesis, I studied the data of two systems for beam position monitoring with different characteristics: DOROS and arc. They provide us independent feedback on the positions during the VdM fill. I modelled the established effects like linear orbit drift, the length scale, and beam-beam deflection and added misalignment into the equation.

This study led to several conclusions. I found that the DOROS and arc systems measure similar values of the linear orbit drift, although at times shifted considerably. DOROS is directly sensitive to the nominal positions, with a mostly consistent length

scale over different scan types. But also arc consistently measures motion that correlates with the nominal positions, telling us that the movement during the VdM fill leaks outside the interaction region. Whether misalignment is present is unclear, except for one beam in the DOROS measurement. The question remains whether that reflects misalignment of the movement or DOROS itself. Finally, I observed beam-beam deflection in the data with a magnitude mostly consistent with theory on average. Significant deviations are, however, present.

Armed with the knowledge of the study above, I performed a VdM scan analysis using the vertex counts of the silicon tracker of CMS. I applied corrections to the moving beam coordinates for orbit drift, beam-beam corrections, and observed residuals. Of all these corrections, the beam-beam deflection most strongly affected the visual cross-section with about a one per cent change. The effect of the residuals is small but suffers from large uncertainty. The beam-beam deflection significantly improves the error on the visual cross-section derived from the VdM fit. The drift correction does not affect the error, while the residuals yield improvement for some scans and worse results for others. Finally, the spread between different VdM scans improves with drift while it remains about the same with the other corrections.

This analysis has far from settled the question of the beam positions. I have, for instance, not considered effects on the position of the non-moving beam. Furthermore, there is no clearly defined method to determine the uncertainty of the residual correction, and the one I used here might still be open to debate. Given the large uncertainties it delivers, one might ask whether this method is overly conservative. However, if not, then the only way forward is to settle the question of how the beam-beam deflection should appear in DOROS and arc systems. If we can do that, one can subtract deflection without fitting it and recover deflection-like drift if present. Finally, the conclusions about the effect on the VdM scans might still change depending on the fit model used in the VdM scans. I noticed that the Gaussian model has some trouble modelling the event rate at large displacements of the beams. A better model could remedy this problem and alter the results of the beam position corrections.

All of these considerations shortly need an answer. This summer, the LHC will enter its third period of data taking, in which it will operate at an unprecedented instantaneous luminosity and is expected to surpass the amount of integrated luminosity collected so far. High instantaneous luminosity enhances several factors limiting accuracy like non-linearity and non-stability, making it more crucial to calibrate even more precisely. That will be even more acute after the third run when the LHC receives an upgrade that should more than double the achievable luminosity.

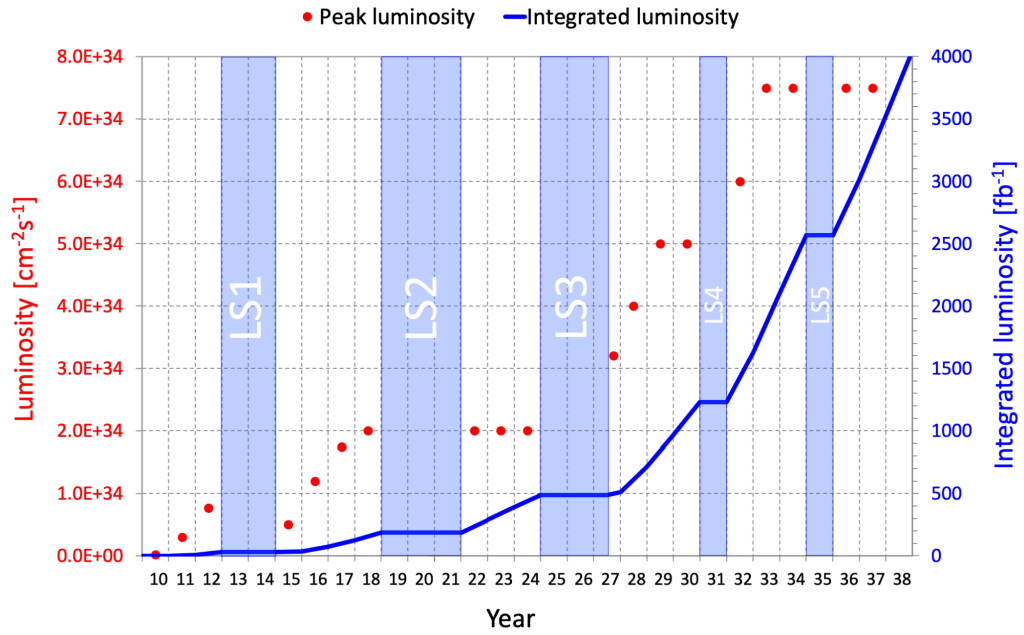


Fig. 6.7.: LHC luminosity forecasts until 2038. Note that the figure is not fully up-to-date: CERN recently decided to extend the third run of LHC by a year and move the third long shutdown (LS3) one year further. More information on <http://lhc-commissioning.web.cern.ch/schedule/LHC-long-term.htm>. Figure from [81].

We will deal with these increased challenges through continued efforts like the one presented in this thesis and new methods that are already under development. The stakes are high, and the opportunities abound. But we will continue to give it our all, make the mists rise ever more, and discover the world spread before us.

Bibliography

- [1]S. Berryman. “Ancient Atomism”. In: *The Stanford Encyclopedia of Philosophy*. Ed. by E. N. Zalta. Winter 2016. Metaphysics Research Lab, Stanford University, 2016 (cit. on p. 1).
- [2]E. Rutherford. “The scattering of α and β particles by matter and the structure of the atom”. In: *Philosophical Magazine* 92 (2012), pp. 379–398 (cit. on pp. 2, 10).
- [3]E. Rutherford. “Collision of α particles with light atoms. IV. An anomalous effect in nitrogen”. In: *Phil. Mag. Ser. 6* 37 (1919), pp. 581–587 (cit. on p. 2).
- [4]C. D. Anderson. “The Positive Electron”. In: *Phys. Rev.* 43 (6 1933), pp. 491–494 (cit. on p. 2).
- [5]C. D. Anderson and S. H. Neddermeyer. “Cloud Chamber Observations of Cosmic Rays at 4300 Meters Elevation and Near Sea-Level”. In: *Phys. Rev.* 50 (4 1936), pp. 263–271 (cit. on p. 2).
- [6]O. S. Brüning, P. Collier, P. Lebrun, et al. *LHC Design Report*. CERN Yellow Reports: Monographs. Geneva: CERN, 2004 (cit. on pp. 2, 15, 16, 18).
- [7]L. Evans and P. Bryant. “LHC Machine”. In: *Journal of Instrumentation* 3.08 (2008), S08001–S08001 (cit. on p. 2).
- [8]S. van der Meer. *Calibration of the effective beam height in the ISR*. Tech. rep. Geneva: CERN, 1968 (cit. on p. 3).
- [9]P. Grafström and W. Kozanecki. “Luminosity determination at proton colliders”. In: *Progress in Particle and Nuclear Physics* 81 (2015), pp. 97–148 (cit. on p. 3).
- [10]G. Aad et al. “Luminosity Determination in pp Collisions at $\sqrt{s} = 7$ TeV Using the ATLAS Detector at the LHC”. In: *Eur. Phys. J. C* 71 (2011), p. 1630. arXiv: 1101.2185 [hep-ex] (cit. on p. 3).
- [11]M. Aaboud et al. “Luminosity determination in pp collisions at $\sqrt{s} = 8$ TeV using the ATLAS detector at the LHC”. In: *Eur. Phys. J. C* 76.12 (2016), p. 653. arXiv: 1608.03953 [hep-ex] (cit. on p. 3).
- [12]G. Aad et al. “Improved luminosity determination in pp collisions at $\sqrt{s} = 7$ TeV using the ATLAS detector at the LHC”. In: *Eur. Phys. J. C* 73.8 (2013), p. 2518. arXiv: 1302.4393 [hep-ex] (cit. on p. 3).
- [13]ATLAS collaboration. “Luminosity determination in pp collisions at $\sqrt{s} = 13$ TeV using the ATLAS detector at the LHC”. In: (June 2019) (cit. on pp. 3, 30).
- [14]LHCb collaboration. “Precision luminosity measurements at LHCb”. In: *Journal of Instrumentation* 9.12 (2014), P12005–P12005 (cit. on p. 3).

- [15] A. M. Sirunyan et al. “Precision luminosity measurement in proton-proton collisions at $\sqrt{s} = 13$ TeV in 2015 and 2016 at CMS”. In: *Eur. Phys. J. C* 81.9 (2021), p. 800. arXiv: 2104.01927 [hep-ex] (cit. on pp. 3, 30, 31, 40, 41).
- [16] CMS Collaboration. *CMS luminosity measurement for the 2017 data-taking period at $\sqrt{s} = 13$ TeV*. Tech. rep. Geneva: CERN, 2018 (cit. on pp. 3, 31, 40).
- [17] CMS Collaboration. *CMS luminosity measurement for the 2018 data-taking period at $\sqrt{s} = 13$ TeV*. Tech. rep. Geneva: CERN, 2019 (cit. on pp. 3, 31, 40).
- [18] V. Papadimitriou. “Luminosity determination at the Tevatron”. In: (2011) (cit. on p. 3).
- [19] A. Tumasyan et al. “Measurement of the inclusive and differential $t\bar{t}\gamma$ cross sections in the dilepton channel and effective field theory interpretation in proton-proton collisions at $\sqrt{s} = 13$ TeV”. In: (Jan. 2022). arXiv: 2201.07301 [hep-ex] (cit. on pp. 3, 25).
- [20] A. Tumasyan et al. “Measurement of the inclusive and differential WZ production cross sections, polarization angles, and triple gauge couplings in pp collisions at $\sqrt{s} = 13$ TeV”. In: (Oct. 2021). arXiv: 2110.11231 [hep-ex] (cit. on pp. 3, 25, 29).
- [21] “Measurement of the mass dependence of the transverse momentum of lepton pairs in Drell-Yan production in proton-proton collisions at $\sqrt{s} = 13$ TeV”. In: (May 2022). arXiv: 2205.04897 [hep-ex] (cit. on pp. 3, 25, 26).
- [22] A. M. Sirunyan et al. “Search for excited leptons in $\ell\ell\gamma$ final states in proton-proton collisions at $\sqrt{s} = 13$ TeV”. In: *JHEP* 04 (2019), p. 015. arXiv: 1811.03052 [hep-ex] (cit. on pp. 5, 6).
- [23] J. R. Oppenheimer, C. N. Yang, C. Wentzel, et al. “Theoretical interpretation of new particles”. In: *6th Annual Rochester Conference on High energy nuclear physics*. 1956, pp. VIII.1–36 (cit. on p. 6).
- [24] A. M. Sirunyan et al. “Search for excited quarks of light and heavy flavor in γ + jet final states in proton-proton collisions at $\sqrt{s} = 13$ TeV”. In: *Phys. Lett. B* 781 (2018), pp. 390–411. arXiv: 1711.04652 [hep-ex] (cit. on p. 6).
- [25] A. Einstein. “Zur Elektrodynamik bewegter Körper”. In: *Annalen der Physik* 322.10 (1905), pp. 891–921. eprint: <https://onlinelibrary.wiley.com/doi/pdf/10.1002/andp.19053221004> (cit. on p. 7).
- [26] A. Einstein. “Ist die Trägheit eines Körpers von seinem Energieinhalt abhängig?” In: *Annalen der Physik* 323.13 (1905), pp. 639–641. eprint: <https://onlinelibrary.wiley.com/doi/pdf/10.1002/andp.19053231314> (cit. on p. 7).
- [27] M. A. Acero et al. “An Improved Measurement of Neutrino Oscillation Parameters by the NOvA Experiment”. In: (Aug. 2021). arXiv: 2108.08219 [hep-ex] (cit. on p. 9).
- [28] K. Abe et al. “Improved constraints on neutrino mixing from the T2K experiment with 3.13×10^{21} protons on target”. In: *Phys. Rev. D* 103.11 (2021), p. 112008. arXiv: 2101.03779 [hep-ex] (cit. on p. 9).
- [29] P. W. Higgs. “Broken symmetries, massless particles and gauge fields”. In: *Physics Letters* 12.2 (1964), pp. 132–133 (cit. on p. 9).

- [30]F. Englert and R. Brout. “Broken Symmetry and the Mass of Gauge Vector Mesons”. In: *Phys. Rev. Lett.* 13 (9 1964), pp. 321–323 (cit. on p. 9).
- [31]ATLAS collaboration. “Observation of a new particle in the search for the Standard Model Higgs boson with the ATLAS detector at the LHC”. In: *Physics Letters B* 716.1 (2012), 1–29 (cit. on p. 9).
- [32]CMS Collaboration. “Observation of a new boson at a mass of 125 GeV with the CMS experiment at the LHC”. In: *Physics Letters B* 716.1 (2012), 30–61 (cit. on p. 9).
- [33]T. Aaltonen, S. Amerio, D. Amidei, et al. “High-precision measurement of the $\langle i \rangle W \langle /i \rangle$ boson mass with the CDF II detector”. In: *Science* 376.6589 (2022), pp. 170–176. eprint: <https://www.science.org/doi/pdf/10.1126/science.abk1781> (cit. on p. 9).
- [34]*The Standard Model | CERN*. <https://home.cern/science/physics/standard-model>. (Accessed on 06/07/2022) (cit. on p. 10).
- [35]M. Aker, A. Beglarian, J. Behrens, et al. “Direct neutrino-mass measurement with sub-electronvolt sensitivity”. In: *Nature Physics* 18.2 (2022), pp. 160–166 (cit. on p. 10).
- [36]S. Eriksson. “Precision measurements on trapped antihydrogen in the ALPHA experiment”. In: *Philosophical Transactions of the Royal Society A: Mathematical, Physical and Engineering Sciences* 376.2116 (2018), p. 20170268 (cit. on p. 10).
- [37]“The indirect search for Dark Matter from the centre of the Galaxy with the Fermi LAT”. In: *Il Nuovo Cimento C* 34.3 (2011), 311–316 (cit. on p. 10).
- [38]N. Agafonova, A. Aleksandrov, O. Altinok, et al. “Observation of a first ν_τ candidate event in the OPERA experiment in the CNGS beam”. In: *Physics Letters B* 691.3 (2010), pp. 138–145 (cit. on p. 10).
- [39]A. Abed Abud, B. Abi, R. Acciarri, and Acero. *Deep Underground Neutrino Experiment (DUNE) Near Detector Conceptual Design Report*. 2021 (cit. on p. 10).
- [40]R. Blair et al. “The CDF-II detector: Technical design report”. In: (Nov. 1996) (cit. on pp. 11, 12).
- [41]B. Pifer et al. “An Experiment at D0 to Study anti-Proton - Proton Collisions at 2-TeV: Design Report”. In: (Dec. 1983) (cit. on pp. 11, 12).
- [42]F. Abe, H. Akimoto, A. Akopian, et al. “Observation of Top Quark Production in $\bar{p}p$ Collisions with the Collider Detector at Fermilab”. In: *Phys. Rev. Lett.* 74 (14 1995), pp. 2626–2631 (cit. on p. 11).
- [43]S. Abachi, B. Abbott, M. Abolins, et al. “Search for High Mass Top Quark Production in $p\bar{p}$ Collisions at $\sqrt{s} = 1.8$ TeV”. In: *Phys. Rev. Lett.* 74 (13 1995), pp. 2422–2426 (cit. on p. 11).
- [44]R. P. Walker. “Synchrotron radiation”. In: (1994) (cit. on pp. 11, 12).
- [45]S. Myers. *The LEP Collider; from design to approval and commissioning*. John Adams’ memorial lecture. Delivered at CERN, 26 Nov 1990. Geneva: CERN, 1991 (cit. on pp. 11, 12).

- [46]E. Regenstreif. “The CERN proton synchrotron. 1.” In: (Aug. 1959) (cit. on p. 12).
- [47]“Report on the design study of a 300 GeV proton synchrotron”. In: (1964) (cit. on p. 12).
- [48]J. Vollaire et al. *Linac4 design report*. Ed. by M. Vretenar. Vol. 6/2020. CERN Yellow Reports: Monographs. Geneva: CERN, Sept. 2020 (cit. on p. 12).
- [49]M. Chanel. “LEIR : The Low-energy ion ring at CERN”. In: *8th European Particle Accelerator Conference (EPAC 2002)*. June 2002, pp. 563–565 (cit. on p. 12).
- [50]M. Brugger et al. “The CLEAR facility at CERN”. In: (2016) (cit. on p. 12).
- [51]S. Chatrchyan, G. Hmayakyan, V. Khachatryan, et al. “The CMS experiment at the CERN LHC”. In: *Journal of Instrumentation* 3.08 (2008), S08004–S08004 (cit. on p. 13).
- [52]G. Aad, E. Abat, J. Abdallah, A. A. Abdelalim, A. Abdesselam, et al. “The ATLAS Experiment at the CERN Large Hadron Collider”. In: *Journal of Instrumentation* 3.08 (2008), S08003–S08003 (cit. on p. 13).
- [53]K. Aamodt, A. A. Quintana, R. Achenbach, et al. “The ALICE experiment at the CERN LHC”. In: *Journal of Instrumentation* 3.08 (2008), S08002–S08002 (cit. on p. 13).
- [54]A. Alves A. A. Augusto et al. “The LHCb Detector at the LHC”. In: *JINST* 3 (2008), S08005 (cit. on p. 13).
- [55]P. Abbon et al. “The COMPASS experiment at CERN”. In: *Nucl. Instrum. Meth. A* 577 (2007), pp. 455–518. arXiv: hep-ex/0703049 (cit. on p. 13).
- [56]A. Ariga et al. “FASER’s physics reach for long-lived particles”. In: *Phys. Rev. D* 99.9 (2019), p. 095011. arXiv: 1811.12522 [hep-ph] (cit. on p. 13).
- [57]E. Lopienska. “The CERN accelerator complex, layout in 2022. Complexe des accélérateurs du CERN en janvier 2022”. In: (2022). General Photo (cit. on p. 13).
- [58]D. I. Kaltchev, M. K. Craddock, R. V. Servranckx, and T. Risselada. “Momentum Cleaning in the CERN LHC”. In: (1998). revised version submitted on 2004-08-20 17:03:58, 4 p (cit. on p. 15).
- [59]A. Alici, G. Anders, N. Bacchetta, et al. “Study of the LHC ghost charge and satellite bunches for luminosity calibration.” In: (2012) (cit. on p. 16).
- [60]P. Forck. *Beam Instrumentation and Diagnostics*. 2020. arXiv: 2009.10411 [physics.acc-ph] (cit. on pp. 17–19).
- [61]G. Anders, N. Bacchetta, V. Balagura, et al. “Study of the relative LHC bunch populations for luminosity calibration”. In: (2012) (cit. on p. 17).
- [62]C. Barschel, M. Ferro-Luzzi, J. J. Gras, et al. “Results of the LHC DCCT Calibration Studies”. In: (2012) (cit. on p. 17).
- [63]M. Gašior, G. Baud, J. Olexa, and G. Valentino. “First Operational Experience with the LHC Diode ORbit and OScillation (DOROS) System”. In: (2017), MOPG07. 4 p (cit. on p. 18).

- [64]Wikipedia contributors. *Quadrupole magnet* — *Wikipedia, The Free Encyclopedia*. [Online; accessed 3-June-2022]. 2022 (cit. on p. 20).
- [65]Vidal, X. C. and Manzano R. C. *Magnetic multipoles*. [Online; accessed 3-June-2022]. 2022 (cit. on p. 20).
- [66]H. Wiedemann. “Single Particle Dynamics”. In: *Particle Accelerator Physics*. Cham: Springer International Publishing, 2015, pp. 177–211 (cit. on p. 19).
- [67]H. Wiedemann. “Particle Beams and Phase Space”. In: *Particle Accelerator Physics*. Cham: Springer International Publishing, 2015, pp. 213–251 (cit. on p. 20).
- [68]M. Hostettler et al. “Comparison of Transverse Emittance Measurements in the LHC”. In: *8th International Particle Accelerator Conference*. May 2017 (cit. on p. 21).
- [69]G. Trad, G. Baud, E. Bravin, et al. “Status of the beam profile measurements at the LHC”. In: *6th Evian Workshop on LHC beam operation*. Geneva: CERN, 2016, pp. 163–170 (cit. on p. 21).
- [70]R. Jones. “Measuring Tune, Chromaticity and Coupling”. In: May 2020. arXiv: 2005.02753 [physics.acc-ph] (cit. on p. 22).
- [71]R. Calaga, R. Miyamoto, R. Tomas, and G. Vanbavinckhove. “ β^* measurement in the LHC based on K-modulation”. In: *Conf. Proc. C 110904* (2011). Ed. by C. Petit-Jean-Genaz, pp. 1864–1866 (cit. on p. 22).
- [72]R. Alemany-Fernández et al. “Cross-Calibration of the LHC Transverse Beam-Profile Monitors”. In: *Proc. of International Particle Accelerator Conference (IPAC’17), Copenhagen, Denmark, 14-19 May, 2017* (Copenhagen, Denmark). International Particle Accelerator Conference 8. <https://doi.org/10.18429/JACoW-IPAC2017-MOPAB130>. Geneva, Switzerland: JACoW, 2017, pp. 437–440 (cit. on pp. 22, 51).
- [73]J. Knolle. *Precision luminosity measurement with proton-proton collisions at the CMS experiment in Run 2* (cit. on p. 25).
- [74]E. Bravin, B. Dehning, G. Ferri, A. Forsstrom, and M. Merkel. “Luminosity measurements at LEP”. In: (1997), 7 p (cit. on p. 29).
- [75]G. Aad et al. “Measurement of the transverse momentum distribution of Drell–Yan lepton pairs in proton–proton collisions at $\sqrt{s} = 13$ TeV with the ATLAS detector”. In: *Eur. Phys. J. C* 80.7 (2020), p. 616. arXiv: 1912.02844 [hep-ex] (cit. on p. 29).
- [76]V. Balagura. “Van der Meer scan luminosity measurement and beam–beam correction”. In: *Eur. Phys. J. C* 81.1 (2021), p. 26. arXiv: 2012.07752 [hep-ex] (cit. on p. 33).
- [77]P. Bambade, R. Erickson, W. A. Koska, et al. “Observation of beam-beam deflections at the interaction point of the SLAC Linear Collider”. In: *Phys. Rev. Lett.* 62 (25 1989), pp. 2949–2952 (cit. on p. 35).
- [78]W. Kozanecki, T. Pieloni, and J. Wenninger. “Observation of Beam-beam Deflections with LHC Orbit Data”. In: (2013) (cit. on p. 35).
- [79]E. Keil. “Beam-beam dynamics”. In: (1994), 16 p (cit. on p. 35).

- [80]A. Chmielinska, L. Fiscarelli, E. Todesco, and W. Kozanecki. “Magnetic measurements of MCBC and MCBY orbit correctors under special cycling conditions”. In: (2022) (cit. on p. 36).
- [81]CMS Collaboration. *The Phase-2 Upgrade of the CMS Data Acquisition and High Level Trigger*. Tech. rep. This is the final version of the document, approved by the LHCC. Geneva: CERN, 2021 (cit. on p. 67).

List of Figures

1.1	The particles of the standard model. Figure from [34].	10
1.2	A schematic overview of the CERN infrastructure and experiments (not to scale). Figure from [57].	13
2.1	Schematic layout of the LHC. The ring is made of Long Straight Sections (LSS) and arcs with Dispersion Suppressors (DSL and DSR) in between. Figure from [6].	16
2.2	DCCT measurement principle. The alternating fields in both tori cancel each other, such that no current flows through a coil wrapped around both tori. A direct current breaks the symmetry, such that a net field arises and current starts flowing. Figure from [60].	18
2.3	Left: schematic drawing of a button BPM configuration. Right: parts of a button BPM used at LHC. The left part is directed towards the inside of the beam tube. Images from [60].	19
2.4	Left: Field lines of an ideal quadrupole magnet. The forces (blue) are shown for a particle moving away from the reader. Figure from [64]. Right: Focusing combination of quadrupoles. Figure from [65].	20
3.1	An illustration of luminosity for two colliding proton bunches. Figure from [73]	25
3.2	Relative uncertainty on the Drell-Yan pair production cross-section with an invariant mass in the range 76 GeV to 106 GeV as a function of the transverse momentum of the Drell-Yan pair. Luminosity accounts almost exclusively for the error on the central bins. Figure from [21].	26
3.3	Vision of the archer on the targets. The total area A is covered by N targets of cross-section σ . The hit probability is $N\sigma/A$	26
4.1	Displacement caused by coherent beam-beam interaction as a function of the displacement along the X -axis. The bunches are assumed to be factorizable.	36

4.2	The nominal beam position during VdM fill in 2017, or fill 6016. The transverse horizontal (X) and transverse vertical (Y) are shown for beam 1 and 2 separately. Note the breaks in the time axis.	37
5.1	DOROS (left) and arc (right) BPM measurements during the two first VdM scans from fill 6016 in 2017.	44
5.2	Illustration of the different effects affecting the position: length scale factor (red dashed), misalignment (purple dashed-dotted), linear orbit drift (green dotted), beam-beam deflection (red ellipse), and unexplained movement (purple dashed ellipse). The plots are only for illustrative purposes and have been selected because they show pronounced effects. The upper figures show the DOROS measurements with the nominal positions subtracted during a BI scan in the Y plane from fill 6868 in 2018. The lower figures show the arc measurements from a BI scan in the X plane from fill 6016 in 2017. Note that length scale and misalignment in the case of the arc refer to leakage.	45
5.3	Linear orbit drift obtained from linear interpolation between the nominally head-on positions before and after each scan. The scans do not include emittance scans. The dots represents the mean position along the X -axis of beam 1 during the step, while the bars show the spread of the BPM measurements within the step.	47
5.4	Comparison between the arc and DOROS measurements during fill 6016 of the interpolated orbit drift slope δ_{LD} and the linear orbit drift interpolated to the scan centre c_{LD} . Every points represents the orbit drift during one scan along one axis for one beam, (e.g. $X1$ during the first VdM scan in the Y plane).	48
5.5	Difference Δ between the arc and DOROS measurements of the positions at the head-on steps before and after each scan as a function of the time elapsed since the last optimisation scan. The lines represent the orbit drift interpolation during the scan. Error bars represent the errors on Δ derived from the spread on the BPM measurements within each step.	48
5.6	Length scale factors for fill 6016 and fill 6868. The vertical bands represent a 1σ confidence interval for average of all scans weighted the fit uncertainties. Note that every displayed point for a given beam coordinate (say $X1$) corresponds to a scan in which there was nominal movement along that coordinate.	50

5.7	Misalignment factors for fill 6016 and fill 6868. The vertical bands represent a 1σ confidence interval for average of all scans weighted the fit uncertainties. Note that every displayed point for a given beam coordinate (say $X1$) corresponds to a scan in which there was nominal movement along the beam coordinate perpendicular to it (i.e. $Y1$).	52
5.8	Modifying factors of the beam-beam deflection for fill 6016 and fill 6868. The vertical bands represent a 1σ confidence interval for the average of all scans weighted by the fit uncertainties. The dashed ligns show the 1σ interval for the expected value $\gamma_D\gamma_G$. Note that every displayed point for a given beam coordinate (say $X1$) corresponds to a scan in which there was nominal movement and thus deflection along that coordinate.	53
5.9	Residuals from the arc data versus those of the DOROS data. The left plot shows the residuals grouped by scan type, the right plot grouped by beam coordinate. Each group has been given an offset along the vertical axis. The diagonal dashed line is shown for reference.	54
5.10	Residuals from the arc data versus those of the DOROS data and their 3σ covariance ellipse. The left shows residuals from fill 6016, the right from fill 6868. The length of the ellipse half axes are displayed.	55
5.11	Residuals of arc and DOROS data from the VdM scans in fill 6016. Only the beam coordinates for which there is also nominal movement are considered. The colored bands are errors derived from the fit. The dashed line shows the average residuals over the different scans. The horizontal axis shows the step number.	56
6.1	VdM scans for fill 6016 with vertex counts recorded in one pair of colliding bunches (BCID 41) by the CMS silicon tracker. The displayed VdM scans use uncorrected nominal positions. The upper row are the VdM scans along the X -axis, the lower row along the Y -axis. The points are the measured average number of vertices per crossing normalised to the product of the proton numbers in each bunch. The dashed lign is a Gaussian function fitted to this data. The values for the width $\Sigma_{X,Y}$ of this Gaussian are shown for each scan.	58
6.2	Calculated values of σ_{vis} based on average number of vertices per crossing for all recorded bcmds in fill 6016. For every bcmd, there are four values corresponding to the four VdM scans performed during this fill. A 1σ confidence interval is shown for the weighted average.	59

6.3	Effect on the values of σ_{vis} from fill 6016 when the positions are corrected for linear orbit drift (+LD), and for beam-beam deflection (+BB). The left shows σ_{vis} itself, the middle the error $d\sigma_{\text{vis}}$, and the right the spread S of σ_{vis} over the four scan pairs. All three quantities are expressed a percentage change relative to their value if no corrections (None) are applied. The full lines on the left two plots show the four σ_{vis} estimates derived from bcid 41. The dashed starred lines shows the average $\bar{\sigma}_{\text{vis}}$ over all scan pairs and bcids, with the error on $\bar{\sigma}_{\text{vis}}$ computed as in equation (5.2).	61
6.4	Effect on the values of σ_{vis} due to subsequent correction for residuals from DOROS (+D), arc (+A), and their average residuals (+M). The left shows σ_{vis} itself, the middle the error $d\sigma_{\text{vis}}$, and the right the spread S of σ_{vis} over the four scan pairs. All three quantities are expressed a percentage change relative to their value if only a LD and BB correction is applied (None). The dashed starred lines shows the average $\bar{\sigma}_{\text{vis}}$ over all scan pairs and bcids, with the error $\bar{\sigma}_{\text{vis}}$ computed as in equation (5.2).	62
6.5	Calculated values of σ_{vis} based on average number of vertices per crossing for all recorded bcids in fill 6868. For every bcid, there are four values corresponding to the four VdM scans performed during this fill. A 1σ confidence interval is shown for the weighted average. . . .	64
6.6	Effect on the values of σ_{vis} from fill 6868 when the positions are corrected for linear orbit drift (+LD), beam-beam deflection (+BB), and residuals (+Res). The left shows σ_{vis} itself, the middle the error $d\sigma_{\text{vis}}$, and the right the spread S of σ_{vis} over the four scan pairs. All three quantities are expressed a percentage change relative to their value if no corrections (None) are applied. The full lines on the left two plots show the four σ_{vis} estimates derived from bcid 265. The dashed starred lines shows the average $\bar{\sigma}_{\text{vis}}$ over all scan pairs and bcids, with the error on $\bar{\sigma}_{\text{vis}}$ computed as in equation (5.2).	64
6.7	LHC luminosity forecasts until 2038. Note that the figure is not fully up-to-date: CERN recently decided to extend the third run of LHC by a year and move the third long shutdown (LS3) one year further. More information on http://lhc-commissioning.web.cern.ch/schedule/LHC-long-term.htm . Figure from [81].	67
A.1	Nominal positions in fill 6016.	83
A.2	Measurements of the DOROS BPM system in fill 6016.	83
A.3	Measurements of the arc BPM system in fill 6016.	84

A.4	Nominal positions in fill 6868.	84
A.5	Measurements of the DOROS BPM system in fill 6868.	85
A.6	Measurements of the arc BPM system in fill 6868.	85

List of Tables

- 4.1 Contributions to the errors of the CMS luminosity measurement in 2015-2016. The upper half (normalization) refers to the σ_{vis} measurement, while the lower half (integration) shows all uncertainty that arises in using the luminometers over an extended time period. Table from [15]. 41

Beam position monitors data



A.1 Beam positions during fill 6016

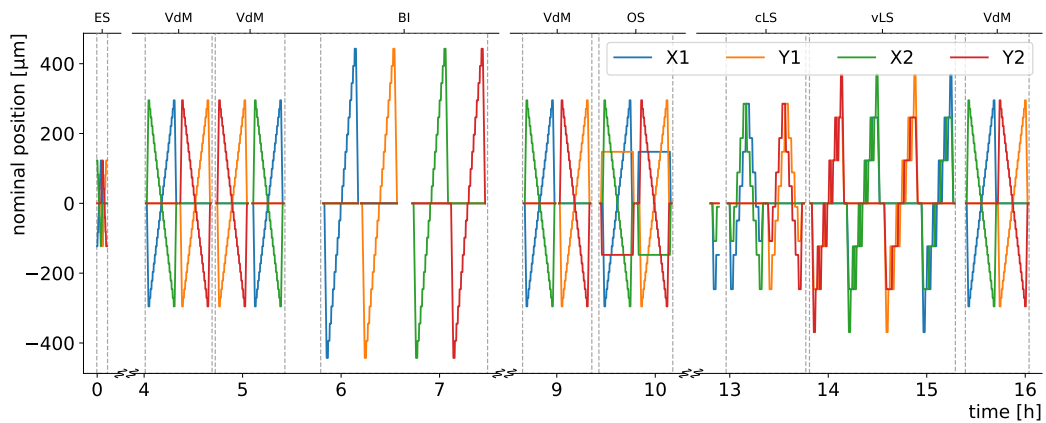


Fig. A.1.: Nominal positions in fill 6016.

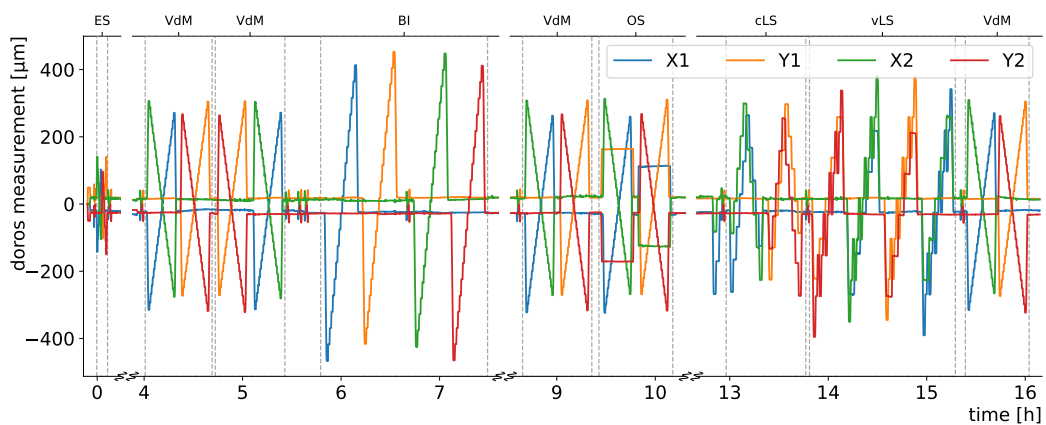


Fig. A.2.: Measurements of the DOROS BPM system in fill 6016.

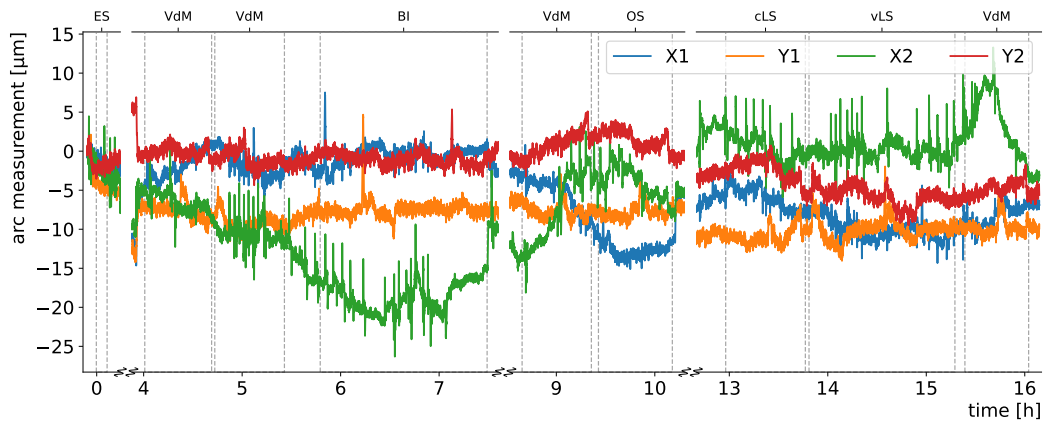


Fig. A.3.: Measurements of the arc BPM system in fill 6016.

A.2 Beam positions during fill 6868

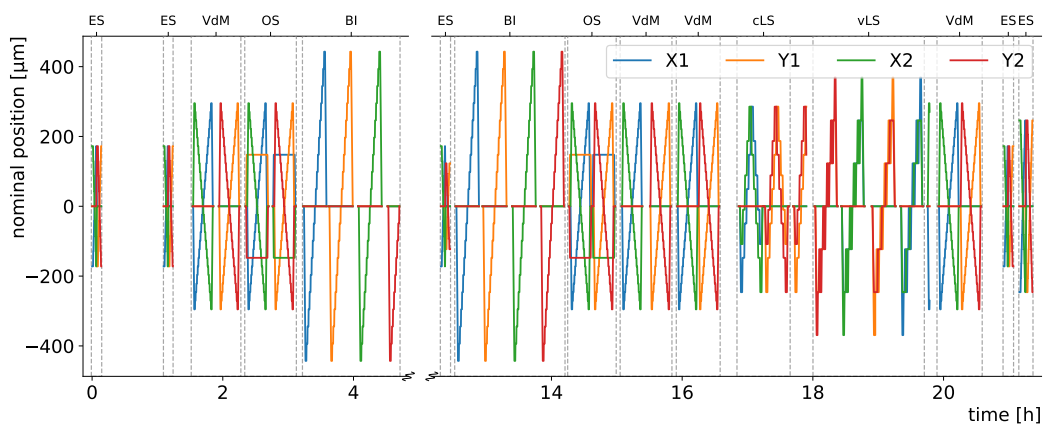


Fig. A.4.: Nominal positions in fill 6868.

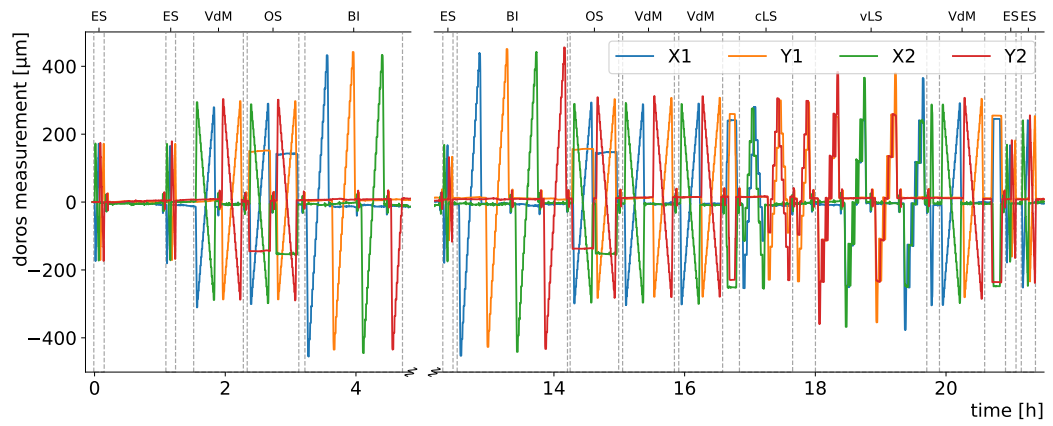


Fig. A.5.: Measurements of the DOROS BPM system in fill 6868.

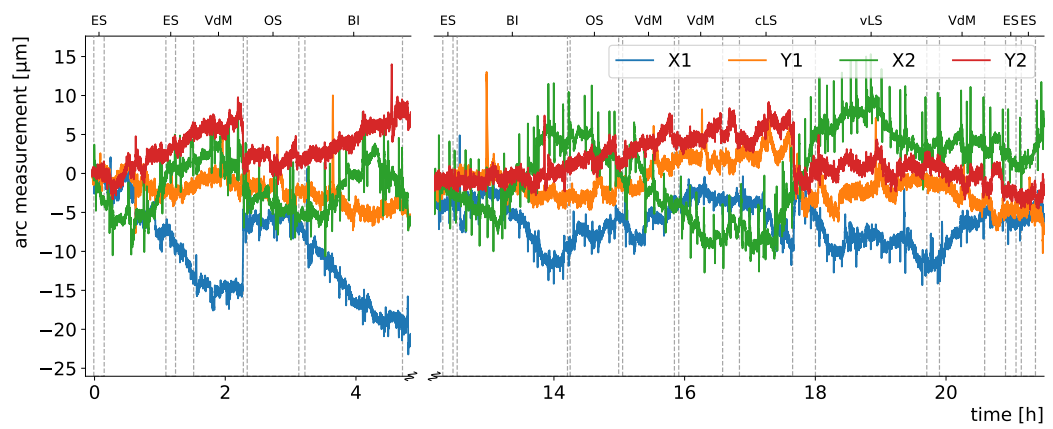


Fig. A.6.: Measurements of the arc BPM system in fill 6868.

Colophon

This thesis was typeset with \LaTeX . It uses the *Clean Thesis* style developed by Ricardo Langner. The design of the *Clean Thesis* style is inspired by user guide documents from Apple Inc.

Download the *Clean Thesis* style at <http://cleanthesis.der-ric.de/>.

Declaration

I declare that I have developed and written the enclosed master's thesis completely by myself, and have not used sources or means without declaration in the text. Any thoughts from others or literal quotations are clearly marked. The master's thesis was not used in the same or in a similar version to achieve an academic grading or is being published elsewhere.

Ghent, Academic year 2021–2022

Maarten De Coen

